Research Article

Arman Hoseinpur*, Stefan Andersson, Michael Müller, Kai Tang, and Jafar Safarian

Boron removal from silicon melt by gas blowing technique

https://doi.org/10.1515/htmp-2022-0011
received July 19, 2021; accepted November 05, 2021

Abstract: Due to the detrimental effects of boron (B) on the efficiency of silicon (Si) photovoltaic cells, complete boron removal from Si is necessary to produce solar grade Si (SoG–Si, with a maximum limit of 0.1 ppmw boron). Gas refining is a promising technique for boron removal from Si, in which the thermodynamic equilibrium never establishes. Hence, by starting from any B concentration in the melt, the required limit for SoG–Si will be achieved. This research is devoted to studying the refractory interactions' effect with melt and the chamber atmosphere on boron removal. For this purpose, gas refining experiments were carried out in alumina and graphite crucibles with H_2 and H_2–3% H_2O refining gases. Gas refining in Ar, He, and continuous vacuuming conditions were also carried out to study the effect of chamber atmosphere. The gas refining results are supported by the characterization of the evaporated species by molecular beam mass spectroscopy (MBMS) technique. The MBMS measurements indicated that the boron evaporation occurs by the formation of the volatile species BH_x, BO_y, and $B_zH_xO_y$ compounds. Most of these compounds are already known in the literature. However, HBO, HBOH, and AlBO (in the case of alumina refractories) were measured experimentally in this work. Results indicate that the evaporation of B in the form of $AlBO_x$ compounds leads to higher mass transfer coefficients for boron removal in alumina crucibles. Density-functional theory (DFT) and coupled cluster calculations are carried out to provide a thermodynamic database for the gaseous compounds in the H–B–O–Al system, including enthalpy, entropy, and C_P values for 21 compounds.

Keywords: boron, SoG–Si, gas refining, hydrogen, kinetics, DFT calculations

1 Introduction

Power production by photovoltaic (PV) panels has increased almost ten times over the past decade and will continue rising in the future [1–3]. More than 90% of the PV panels are produced from silicon (Si) [4]. The Si for PV applications must have a purity degree of 6N (99.9999%), known as solar grade Si (SoG–Si). Among all the impurities that should be removed from Si to reach the SoG–Si, boron (B) is one of the most harmful elements to exist, which will reduce the efficiency of the PV modules. Boron exists in the metallurgical grade Si (MG–Si) in tens of ppmw, while a maximum limit of only 0.1 ppmw is acceptable for SoG–Si. Most metallic impurities can be removed from MG–Si through the directional solidification technique – the last key step in ingot production for solar cells. However, B has a high segregation coefficient (0.8), making it impossible to be separated from Si by the directional solidification technique. Therefore, reliable methods are required for B removal from Si.

The most important metallurgical methods investigated for B removal from Si applied till now are slag refining [5–7], plasma refining [8–12], and gas refining techniques [13–16]. Slag refining is a well-established process for B removal from Si, and is industrialized by Elkem®. In slag refining, the Si melts are equilibrated with slags which absorb B from the liquid Si. Teixeira and Morita [17] reported a boron removal degree as high as almost 85% applying SiO_2 and CaO slag system (where slag over Si weight ratio was 2.23). However, Jakobsson and Tangstad [18] and Jakobsson [19] reported lower degrees of boron removal by the same slag system (almost 73% for slag over Si weight ratio of unity could be achieved in this technique). This means reaching to the SoG–Si limit depends on the initial B content of the melt.

* **Corresponding author: Arman Hoseinpur,** Department of Materials Science and Engineering, Norwegian University of Science and Technology (NTNU), 7034 Trondheim, Norway,
e-mail: arman.h.kermani@ntnu.no
Stefan Andersson, Kai Tang: SINTEF Industry, 7465 Trondheim, Norway
Michael Müller: Institute of Energy and Climate Research, IEK-2, Forschungszentrum Jülich GmbH, Wilhelm-Johnen-Straße, 52428 Jülich, Germany
Jafar Safarian: Department of Materials Science and Engineering, Norwegian University of Science and Technology (NTNU), 7034 Trondheim, Norway

However, in the gas refining process, the refining gases are blown over the melt surface to remove B from liquid Si in the form of the volatile B species such as: boron oxides (B_xO_y), boron hydrides (BH_x), and boron oxyhydroxides ($B_xO_yH_z$). In the gas refining process, the thermodynamic equilibrium never establishes, and B can be continuously removed from the liquid Si. This can be regarded as an advantage of gas refining process over the slag refining. In addition, the slag leftover from the slag refining process is a solid waste which then imposes costs for being disposed, especially if the environmental issues must be met in the production site. At the same time, the only by-product of the gas refining is silica fumes (SiO_2), which have applications in cement and concrete production [20–22]. Plasma refining of Si is also a method resembling gas refining in terms of removing the B species by oxidizing and removing in the form of volatile species, but totally different in physics and power consumption is high in the process.

Boron removal by plasma technique was studied by Baba et al. [23] by applying water vapor and then was further investigated by Nakamura et al. [11] and Alemany et al. [12]. Wu et al. [24] reported the gas refining without plasma torch in an electric arc furnace with $Ar–H_2O–O_2$ gas mixtures. From 2012 the gas refining of Si by humidified hydrogen was initiated in NTNU [25,26], by applying an induction furnace and top gas blowing technique. The gas mixture of interest for the NTNU researchers has always been a combination of H_2–x% H_2O, which leads to high mass transfer coefficient values for B removal and then higher rates of the process. When applying oxidative gases like O_2 and H_2O, the surface of Si melt oxidizes, and if the surface oxide layer becomes thick, then the evaporation kinetics slow down. The surface passivation of liquid Si is studied in the oxidative plasma refining technique by Vadon et al. [27]. A right selection of the H_2/H_2O can prevent surface oxidation, and previous studies showed that the maximum process rate could be achieved when x = 3–4%. Safarian et al. [28] compared the effect of addition of Ar and He to the H_2–4% H_2O and showed that Ar addition reduces the rate of B removal while showing a better result. The mechanism of B removal from Si is mainly known by the formation of $B_xO_yH_z$ compounds and among them, the HBO is known to contribute to B removal from Si more than any other compound, due to its higher vapor pressure [27–29]. The following reaction is suggested for the formation of HBO:

$$\underline{B} + \underline{H} + \underline{O} = HBO_{(g)}, \quad (1)$$

where $\underline{B}$, $\underline{H}$, and $\underline{O}$ are the dissolved boron, hydrogen, and oxygen in liquid Si. The effect of the refractory–melt interaction was studied by Safarian et al. [30], reporting the privilege of oxide crucibles (alumina and quartz) over the graphite crucibles leading to higher rates of B removal. When using graphite crucibles, the carbon dissolved in liquid Si will reduce the dissolved oxygen from the gas to form $CO_{(g)}$, and hence the concertation of $\underline{O}$ is lower compared to oxide refractories (quartz and alumina). However, when comparing alumina with quartz, alumina provides higher B removal rates from liquid Si. Safarian et al. [30] suggested the evaporation of B species in the form of $AlBO_2$ compound in case of alumina crucibles but did not present experimental characterizations of the gas phase. The following reaction is suggested for the formation of volatile aluminum oxyboride compound, contributing to B removal in alumina crucibles [30]:

$$\underline{Al} + \underline{B} + 2\underline{O} = AlBO_{2(g)}. \quad (2)$$

The effect of gas flow rate (for $H_2–H_2O$ gas mixtures) and the gas stream pattern was studied by Sortland and Tangstad [31], and Safarian et al. [30], and they showed that there is a linear relationship between the gas flow rate (Q, NL·min^{-1}) and the mass transfer of the B removal (k_B, m·s^{-1}) process. When carrying out the gas refining process by the top blowing technique, many parameters can act on the process rate such as: gas flow rate, type of gas mixture, the distance of the nozzle from the melt surface, diameter of the nozzle compared to the melt surface diameters, and the melt interaction with the refractory holding liquid Si, all these parameters have been studied to some extent in the previous works. Among all the variables in the gas refining of Si, we study the effect of the interaction of refractory – melt and the chamber bulk gas on the kinetics of B removal. In addition to that, the gaseous species evaporating from the melt were characterized experimentally, to expand our knowledge about the Si refining process.

2 Theoretical thermodynamics of H–Al–B–O system

In order to study the thermodynamics of the system, density-functional theory (DFT) calculations were employed by using the M06-2X density functional [32] and a maug-cc-pV(T+d)Z basis set [33] employing the NWChem code [34], and the thermodynamics data for the following gaseous compounds were generated:

HBO, three isomers of HBOH (H_2BO, *cis*-HBOH, and *trans*-HBOH), H_2BOH, two isomers of AlBO (AlOB and AlBO), $AlBO_2$, BO, BO_2, B_2O_2 BH, BH_2, BH_3, B_2O, B_2O_3, HOBO, $HB(OH)_2$, $B(OH)_2$, $B(OH)_3$, and B_2H_6.

For a majority of these species high-level quantum chemistry calculations using the coupled cluster with single and double excitations and a perturbative treatment of triple excitations (CCSD(T)) method were also performed [35]. For calculating the heat of formation of some key molecular species, we followed a procedure where first the molecular geometry was optimized using CCSD(T) with the basis set aug-cc-pVQZ [36] for H, B, and O and aug-cc-pV(Q+d)Z [37] for Al using the commonly employed frozen-core approximation. For open-shell species unrestricted Hartree-Fock wavefunctions were used as reference states for the CCSD(T) calculations. Subsequently, harmonic vibrational frequencies were calculated using the same method. Using the optimized geometries, frozen-core calculations with CCSD(T) and the larger aug-cc-pV5Z, aug-cc-pV6Z [38], aug-cc-pV(5+d)Z, and aug-cc-pV(6+d)Z [37] basis sets were carried out in order to approach the complete basis set (CBS) limit. The calculated energy was further corrected for core-valence (CV) electron correlation, where not only valence but also outer core electrons (1s for H and O, 2s and 2p for Si) were correlated in the CCSD(T) calculations (using the cc-pwCVTZ, cc-pwCVQZ, and cc-pwCV5Z basis sets) [39]. Both the frozen-core and CV calculations were extrapolated to the CBS limit using the extrapolation formula $E(\mathrm{CBS}) = E(\ell_{\max}) + A/(\ell_{\max} + 1/2)^4$ [40,41]. Finally, a first-order relativistic correction was added by employing all-electron CCSD(T) with an uncontracted cc-pVTZ [42,43] basis set and the direct perturbation theory (DPT2) method [44,45]. All coupled cluster calculations were performed using the CFOUR software package [46].

The enthalpy of formation, standard entropy, and heat capacity were calculated by standard statistical thermodynamics equations employing calculated vibrational frequencies, rigid-rotor rotational constants calculated from the optimized geometries, and experimental data on electronic fine-structure states [47]. The standard states of B and Al at 298 K are the solid state, but for practical reasons the B and Al atoms were used as reference species in the CCSD(T) calculations. We therefore employed the most accurate estimate of the heat of formation of the B and Al atoms available, to adjust the heat of formation to the correct reference value [48].

In Table 1, the enthalpies of formation, standard entropies, and heat capacities calculated with M06-2X and CCSD(T) are given together with literature data. For

Table 1: Thermodynamic data calculated by M06-2X, CCSD(T) [**bold** in brackets], and literature values (in parentheses: *JANAF* (italic) ([49]) and others)

Molecule	ΔH_f^0 (298 K)/kJ·mol^{-1}	S^0 (298 K)/J·kmol^{-1}	C_p (298 K)/J·kmol^{-1}
HBO	−240.18 [**−238.18 ± 5.0**] (*−198.32 ± 3*, −210.63 ± 25[a])	202.40 [**202.85**] (*202.62*, 202.69[a])	34.64 [**35.29**] (*35.26*, 35.31[a])
H_2BO	−84.08 [**−69.13 ± 5.0**]	228.20 [**228.49**]	41.58 [**41.86**]
Cis-HBOH	−75.82 [**−51.78 ± 5.0**]	231.82 [**231.93**]	40.36 [**40.37**]
Trans-HBOH	−80.72 [**−58.68 ± 5.0**]	231.36 [**231.44**]	40.18 [**40.14**]
H_2BOH	−291.64 [**−276.79 ± 5.0**] (−292.88 ± 4.2[b])	230.45 [**230.47**]	41.90 [**41.82**]
AlOB	−45.19 [**−27.55 ± 6.7**]	256.37 [**261.83**]	49.95 [**50.14**]
AlBO	3.99 [**9.09 ± 6.7**]	251.53 [**251.29**]	51.14 [**51.06**]
$AlBO_2$	−547.69 [**−525.22 ± 6.7**] (*−541.41 ± 17*)	276.92 [**281.54**] (*269.56*)	60.81 [**61.50**] (*66.86*)
BO	−0.02 [**9.55 ± 5.0**] (*0 ± 8*, 9.81 ± 11[a], 25[c])	203.39 [**203.54**] (*203.48*, 203.47[a], 203.5[c])	29.16 [**29.18**] (*29.20*, 29.20[a], 29.2[c])
BO_2	−284.54 (*−284.51 ± 8*; −309.13 ± 20[a], −300.4[c])	230.53 (*229.81*, 230.13[a], 229.6[c])	45.21 (*43.28*, 43.28[a], 43.0[c])
BH	442.42 [**443.23 ± 5.0**] (442.67 ± 8.4; 442.7[c])	171.69 [**171.76**] (*171.85*, 171.8[c])	29.11 [**29.11**] (*29.18*, 29.2[c])
BH_2	304.83 [**324.25 ± 5.0**] (*200.83 ± 63*; 318.29 ± 11[a])	194.02 [**194.02**] (*180.19*, 193.55[a])	34.70 [**34.79**] (*34.03*, 34.72[a])
BH_3	86.00 [**102.10 ± 5.0**] (*106.69 ± 10*; 88 ± 10[a], 89.2[c])	188.13 [**188.22**] (*187.88*, 187.69[a], 188.2[c])	35.84 [**35.87**] (*36.22*, 34.78[a], 36.0[c])
B_2O	155.90 [**175.77 ± 5.9**] (*96.23 ± 105*)	241.48 [**256.91**] (*227.75*)	47.15 [**47.32**] (*38.41*)
B_2O_2	−457.07 [**−450.53 ± 5.9**] (*−456.81 ± 8.4*; −457.73 ± 10[a]; −454.8[c])	247.34 [**248.47**] (*242.60*, 249.66[a], 242.5[c])	59.08 [**59.65**] (*57.30*, 60.27[a], 57.3[c])
B_2O_3	−860.46 [**−836.51 ± 5.9**] (*−835.96 ± 4.2*; −843.8[c])	284.82 [**285.87**] (*283.77*, 279.8[c])	65.89 [**66.73**] (*66.86*, 66.9[c])
HOBO	−562.00 [**−550.98 ± 5.0**] (*−560.66 ± 4.2*; −561.9[c])	242.34 [**243.01**] (*239.73*, 240.1[c])	47.03 [**47.43**] (*42.23*, 42.2[c])
$HB(OH)_2$	−666.45 (−643.50 ± 8.4[b])	255.63	55.03
$B(OH)_2$	−446.03 (*−470 ± 15*)	259.57 (*249.02*)	53.71 (*52.02*)
$B(OH)_3$	−1,026.81 (*−992.28 ± 2.5*; −994.1[c])	269.84 (*295.237*)	71.34 (*65.34*)
B_2H_6	10.35 (*41.0 ± 16.7*; 36.6 ± 2.0[a]; 36.4[c])	231.73 (*233.17*, 232.49[a], 232.1[c])	55.44 (*58.10*, 57.57[a], 56.7[c])

[a]Gurvich and Veyts [50]; [b]Porter and Gupta [51]; [c]CODATA [52].

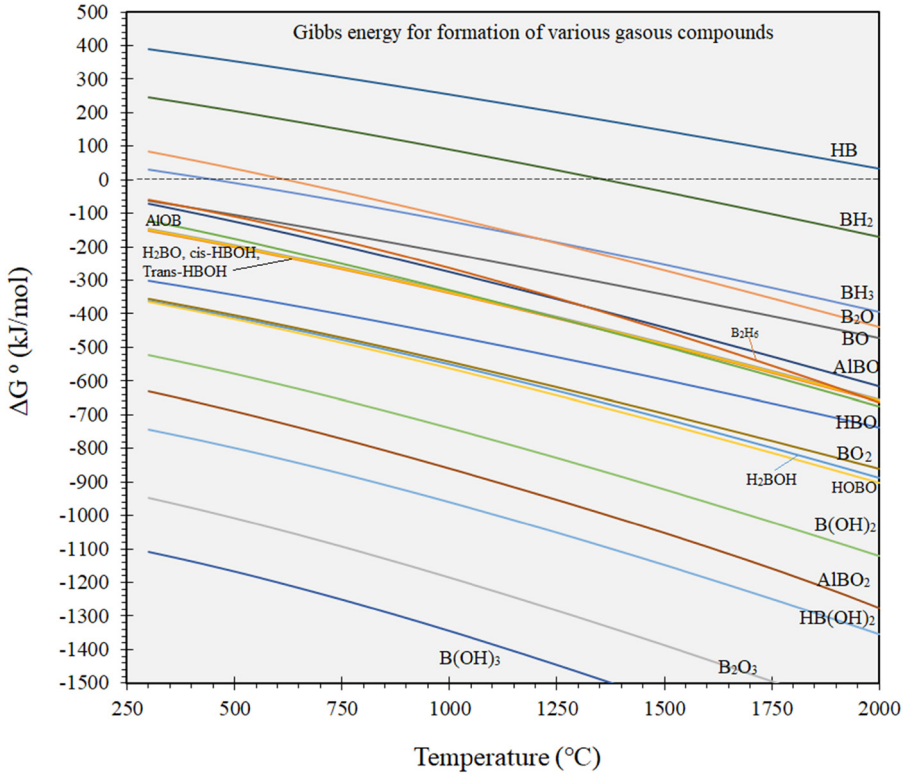

Figure 1: The Gibbs energy for formation of the gaseous compounds in H–Al–B–O system calculated by M06-2X.

H_2BO, *cis*-HBOH, *trans*-HBOH, AlOB, and AlBO there are no literature values of the thermodynamic quantities. In addition, the uncertainties of the literature data are very large for BH_2 and B_2O and fairly large for HBO, $AlBO_2$, BO, BO_2, and BH_3. In these cases, it is recommended to use the calculated CCSD(T) data wherever available and otherwise the M06-2X data. However, BO_2 has a specific electronic structure in which the electronic wave function has a *multireference character*, for which both standard DFT and coupled cluster calculations are less well-suited. This, at the very least, increases the uncertainty of the results and in certain cases makes the results non-trustworthy. Since it is possible to estimate the uncertainty in the calculated enthalpy of formation of the CCSD(T) calculations for "well-behaved" systems, the CCSD(T) results for BO_2 are not included here exactly because it is not possible to make valid estimates of the uncertainty. The calculated parameters based on M06-2X and CCSD(T) are presented in the appendix section (Tables A2 and A3). By using the calculated results, the Gibbs free energy for the aforementioned gaseous compounds are calculated and presented in Figure 1. This figure indicates that the boron-oxyhydroxides have a negative value of Gibbs energy for formation over all the temperature ranges, while the boron hydrides get negative values of Gibbs energy only at elevated temperatures (for BH_2 and BH_3). Figure 2 compares the results generated by M06-2X and CCSD(T) for some selected species.

3 Experimental procedure

3.1 Refining experiments

In this research, all the refining experiments were carried out in a vacuum induction furnace with the setup configuration presented in Figure 3. As shown in the figure, Si was melted in graphite (high density, with the properties presented by Hoseinpur and Safarian [53]) or alumina sintered (ALSINT) crucibles. The crucible used for holding material was put in a bigger graphite crucible and a thermocouple type C (W – 6% Re, W – 26% Re, protected by an alumina sheath) was placed in-between the crucibles to measure the temperature of the process. The preliminary experiments with two thermocouples, one in the inner crucible and the second one in-between the two crucibles, indicated that there is only a 2–4°C temperature difference, and hence the gas refining experiments were carried out

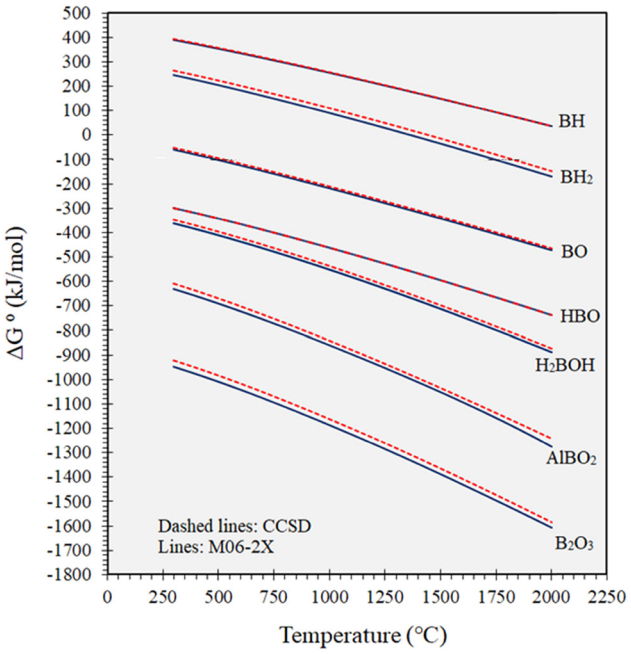

Figure 2: Gibbs free energy for selected gaseous compounds calculated by M06-2X and CCSD(T).

with the thermocouple placed in-between the two crucibles. The inner crucible was charged by 213 g of Si, with a mixture of 50 wt% of polysilicon (FBR®, 8N purity) and 50% Silgrain® (HQ – micron cut; 0.04 wt% Fe, 0.09 wt% Al, 0.013 wt% Ca, 0.001 wt% Ti, 0.085 wt% C, 25 ppmw P, and 30 ppmw B). This mixture provides about 15–20 ppmw B impurity in the initial melt. Before the experiments, the chamber was vacuumed down to 5–7 Pa and flushed by Argon (6N) or Helium (6N) for 3 times. Subsequently, the power was switched on and after the material was melted, a sample was taken from the melt to record the initial composition of the melt. Then, the refining process was started by blowing the refining gas over the Si melt surface, as shown in Figure 3. Table 2 presents the experimental conditions applied for various experiments in this research. The refining gas flow was adjusted by mass flow controller during the experiment and the gas was blown over the melt surface through a quartz lance with a 2 mm nozzle and the nozzle distance to melt surface was kept as 30 mm in all the experiments. In those experiments that humidified hydrogen, which was used as the refining gas, the hydrogen flow was redirected to a gas humidifier unit and then was humidified with 3% H_2O. In order to study the effect of bulk atmosphere in the furnace, in one experiment the chamber was filled with He to compare the results with the experiments where Ar was used to fill the chamber. In addition, in another experiment, the gas refining in vacuum conditions was also studied by blowing the refining gas over the melt surface while the chamber was being vacuumed continuously. In this special experiment, the pressure in the chamber was almost 5 mbar while carrying out the gas refining. Then, the gas blowing was started and several samples were taken from the melt

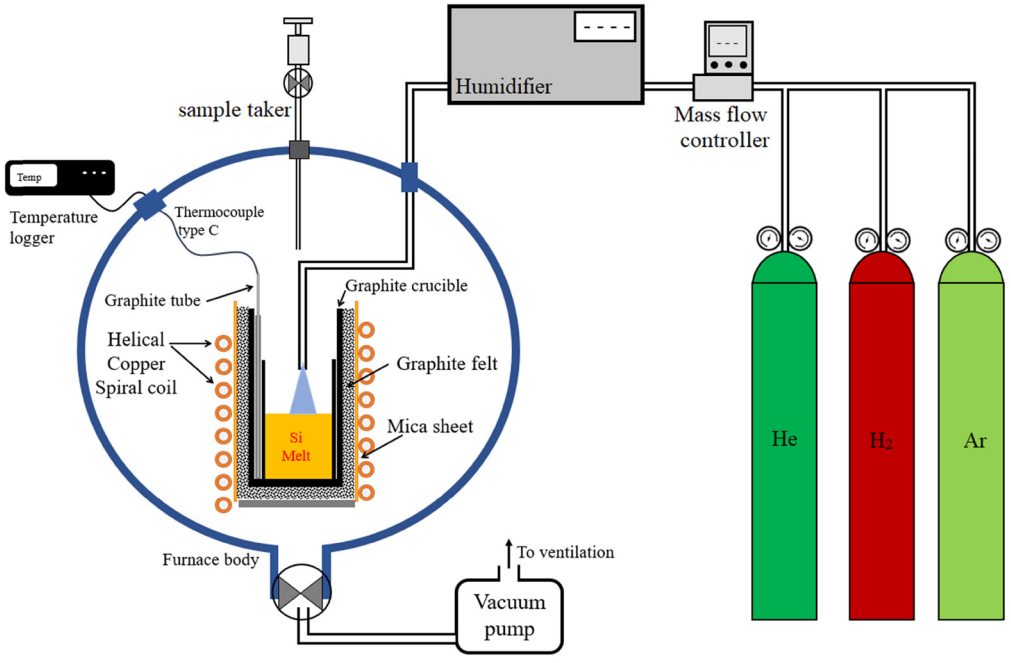

Figure 3: The schematic of the furnace and gas refining set up.

Table 2: The experimental conditions of the gas refining experiments

Crucibles	Alumina, graphite
Refining Gas	H_2–3% H_2O/H_2
Gas flow rate (NL·min^{-1})	3
Chamber bulk gas atmosphere	Ar/He/vacuum
Gas nozzle diameter (mm)	2
Nozzle distance from melt surface (mm)	30
Crucible inner diameter (mm)	50 ± 1
Refining temperature (°C)	1,450, 1,500, and 1,600

during the refining process to track the B concertation change over time. These samples were taken by quartz tubes and later were digested in a mixture of HF and HNO_3 acids, subsequently characterized by inductively coupled plasma mass spectrometry (ICP-MS; Agilent 8800 Triple Quad). When the experiments were done, we shut down the power and let the crucible to cool down by itself. Then, some samples were taken from the fumes settled on the chamber's wall to be characterized by scanning electron microscopy (SEM).

3.2 Molecular beam mass spectrometry (MBMS) characterizations

Hot gas analysis in this study was conducted using MBMS. A detailed description of the system used in this study is given by Wolf et al. [54]. For all the MBMS measurements in this study, the MBMS system has been coupled to a high-temperature reactor shown schematically in Figure 4. A sample boat made of graphite, alumina, or silica containing 2 g of a Si–B (350 ppmw) was attached to the end of an alumina rod and inserted into a tubular alumina reactor with an inner diameter of 21 mm, which was housed in a high-temperature furnace. Before running the experiment, the reactor chamber was flushed with Helium gas for 10 min to reduce the oxygen potential in the chamber, and then the furnace was switched on. The He flow to the chamber was maintained during the experiment. The furnace was maintained at a constant temperature of 1,500°C. The reactor was coupled to the sampling orifice of the MBMS device, to sample the high-temperature gases. The orifice was protruded into the furnace to maintain an elevated temperature to prevent condensation of gas phase species on the tip of the orifice. At the beginning of each experiment, the sample boat was held in the cooled zone of the reactor and a background spectrum was acquired for about 1 min. While the MBMS was kept in a constant scanning mode, the sample boat was inserted into the heated region of the reactor and the evaporated species were monitored over time. During experiments, 5% H_2 in He flowed through the reactor at a flow rate of 4 NL·min^{-1}. The residence time of released vapors in the reactor before sampling was about 0.1 s. Water steam was added after a few minutes via a vaporizer achieving humidity concentrations of 3–5% in the gas stream flowing to the reactor.

Due to the relatively high gas flow necessary to minimize ambient air leaking into the reactor at the connection between furnace and MBMS, vaporization is unlikely to reach equilibrium. Therefore, the gas flow was stopped for about 20 s in some measurements to locally increase the concentration of vapor species above the sample boat. After switching on the gas again, high intensity peaks for qualitative analysis could be recorded. Because of this procedure, the present results are of a rather qualitative nature and therefore, released species were not quantified.

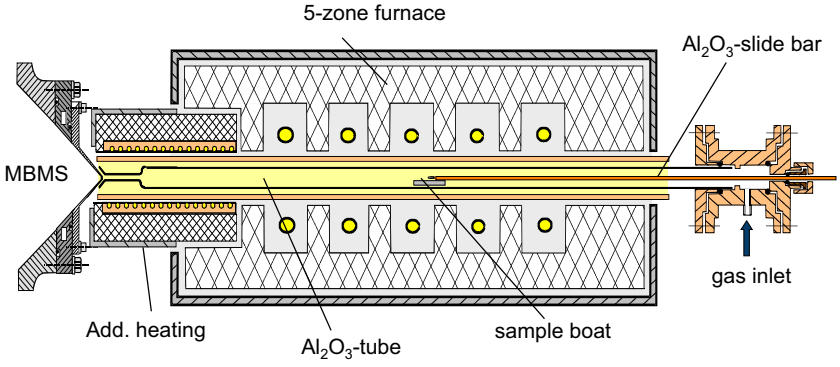

Figure 4: Setup used for vaporization experiments, from Wolf et al. [54].

The mass-to-charge ratio (m/z) range of 5–100 was subjected to a preliminary scan via MBMS to determine the major compounds. The ions of interest and their corresponding m/z ratio are all mentioned in Table 3. It should be mentioned that either ions originate from gas molecules or fragmentation within the ionization region of the MS. For example, B^+ can originate from any B containing gas molecule. Unfortunately, not all masses could be properly recorded due to superimposing of species with the same m/z originating from background or small amounts of ambient air. For example, N_2^+ (m/z 28) superimposes BOH^+ and Si^+ on the same m/z. Furthermore, m/z with too high signal intensity, e.g., 44 (SiO^+ and CO_2^+ from background) had to be excluded to prevent an overload of the multiplier.

4 Results and discussions

4.1 Rate of B removal in gas refining experiments

The B concertation in liquid Si was measured by ICP-MS and all the results are presented in Table A1 (in appendix section). To study the rate of B removal under experimental conditions, the first-order kinetic model was applied, presented here as follows:

Table 3: The ions of interest studied in the MBMS and their corresponding m/z ratio

Ion	m/z
B^+	10, 11
BH^+	11, 12
BH_2^+	12, 13
HBO_2^+	43, 44
BH_3^+	13, 14
BO^+	26, 27
HBO^+	27, 28
$H^{11}B^{18}O^+$	30
$HBOH^+$	29
B_2O^+	36, 38
BO_2^+	42, 43
$B_2O_2^+$	52, 54
$AlBO^+$	53, 54
$B_2O_3^+$	68, 70
$AlBO_2^+$	69, 70

$$\ln\left(\frac{[\text{B wt\%}]_0}{[\text{B wt\%}]_t}\right) = k_B\left(\frac{A_{\text{melt surface}}}{V_{\text{melt}}}\right)t, \quad (3)$$

where t denotes time in seconds, the $[\text{B wt\%}]_0$ and $[\text{B wt\%}]_t$ are the B concentrations in liquid Si at initial time and at time t, respectively. A/V is the surface to volume ratio of melt in (m^{-1}), and k_B is the overall mass transfer coefficient of B removal in the experiments. The calculated k_B for various experimental conditions are presented in Table 4.

4.2 MBMS measurements

The results from the MBMS measurements are all presented in Figure 5. This figure represents the gaseous species that were detected in the gas phase when having liquid Si in quartz, graphite, and alumina boats. In Figure 5, the intensity of the detected species in each sample is normalized based on the sharpest peak. Figure 5(a) shows the B species in He – 5% H_2 gas stream without any humidity added to the gas. As mentioned before, the sample was inserted into the chamber after 10 min of He – 5% H_2 flushing and hence, it is expected to have oxygen partially present in the chamber. From Figure 5(a) it is clear that the major B species detected in all the samples are BH_x compounds. However, when comparing the graphite and quartz boats, it is clear that there are more B_xO_y compounds with higher intensities in the case of quartz boat. As can be seen in Figure 5(a), in the case of quartz boat, the BO_2^+ compound had the second highest intensity after BH_2. From Figure 5(a) it is obvious that when alumina boat is applied, the new $AlBO^+$ compound is detected by MBMS, which indicates the positive role of Si melt interaction with alumina leading to the formation of new volatile B compounds. In addition to all the B_xH_z, $B_xH_yO_z$, and B_xO_y compounds, the B^+ ion is obvious in Figure 5(a). It is worth mentioning that B has a very low vapor pressure [31] and the direct evaporation of B from Si is not assumable. The authors have already studied the vacuum evaporation for Si having P and B concertation of about 10–15 ppmw in the initial melt, and they never detected any B evaporation even in vacuum conditions. Figure 5 shows that the BH_x compounds have the highest intensities, while the thermodynamic calculations indicated that these compounds have higher Gibbs free energy than the other B containing species. Hence, we believe that the B^+ and BH_x^+ ions detected in all cases are mainly the results of fragmentation of bigger molecules in the ionization chamber of MBMS. In addition, Figure 5(b) depicts the detected gaseous species in the gas phase when humidity (3–5%) was added to the gas stream. As it is obvious from this figure that many of the B_xO_y peaks (in case of quartz boat) and the

Table 4: The results from gas refining in various crucibles

Experiment code	Crucible	Temperature (°C)	Chamber atmosphere	Blowing gas	k_B (μm·s^{-1})
1	Graphite	1,500	Ar	H_2	0.9
2	Graphite	1,500	Ar	H_2–3% H_2O	13
3	Graphite	1,500	He	H_2–3% H_2O	17.3
4	Graphite	1,500	Vacuuming (5 mbar)	H_2–3% H_2O	Apparent = 2.56 and effective = 23.3
5	Alumina	1,450	Ar	H_2	1.64
6	Alumina	1,500	Ar	H_2	4.15
7	Alumina	1,600	Ar	H_2	4.96
8	Alumina	1,600	Ar	H_2–3% H_2O	15.3

Apparent: the k_B is calculated by assuming the surface of melt without impinging as the gas – melt contact area. Effective: the k_B is calculated by assuming the surface of impinged point as the gas – melt contact area.

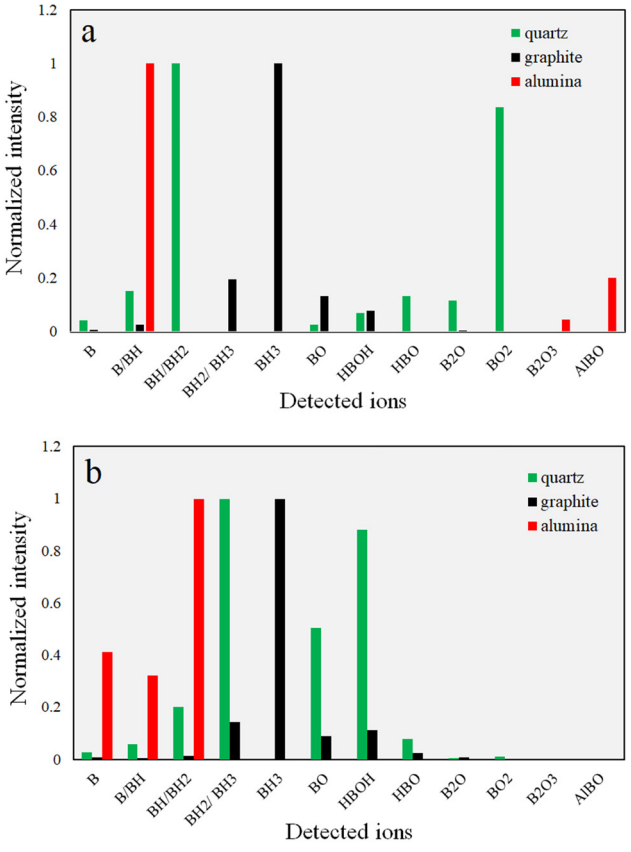

Figure 5: The measured species in MBMS results: (a) He – 5% H_2, (b) He – 5% H_2 humidified with 3–5% H_2O. (Detected oxide compounds in (a) is due to partial pressures of oxygen remaining in the chamber).

$AlBO^+$ peak (in case of the alumina boat) have vanished or have lost their intensities. In the experiment with the graphite and quartz boats, it can be seen that when the humidity was added, the intensity of the compound $HBOH^+$ was increased in both cases, but the $HBOH^+$ compound was detected with higher intensities in the alumina case. $HBOH^+$ is detected as a new compound in this study and previously was proved only to exist by theoretical calculations [55]. It is previously discussed and shown that the concertation of O is lower in graphite crucibles compared to alumina crucibles due to the formation of $CO_{(g)}$, and this can explain the higher intensities of the $HBOH^+$ compound detected when quartz boat was used [31,56].

The B removal from Si melt takes place by formation of HBO compound. We can assume the formation of HBOH in gas refining through the following reaction:

$$\underline{B} + \underline{O} + 2\underline{H} = HBOH_{(g)}. \quad (4)$$

However, the thermodynamics calculations presented in Figure 1 indicated that there are other molecules than HBO and HBOH having considerable negative values of Gibbs energy, such as $B(OH)_3$, $HB(OH)_2$, and B_2O_3, but none of these compounds were detected in the MBMS measurements. This could be due to the need for several elements to reach together at the melt surface and form the aforementioned molecules, which reduces the formation chance of these molecules.

Considering the discussions presented in Section 1 and here, the mechanisms of B removal from liquid Si with H_2–H_2O gases is schematically summarized in Figure 6. This figure shows that an important step in the process is the dissolution of the H and O in the liquid Si from gas phase. When quartz and alumina crucibles are applied, O and Al can also be dissolved from the crucibles, while in case of graphite crucibles, C will be dissolved from graphite crucible. Formation of solid silicon oxide on melt surface is also obvious from this illustration.

4.3 Effect of crucible interactions with melt on B removal

A comparison between the experiments (1) with (2) shows that when dry hydrogen was used as the refining gas,

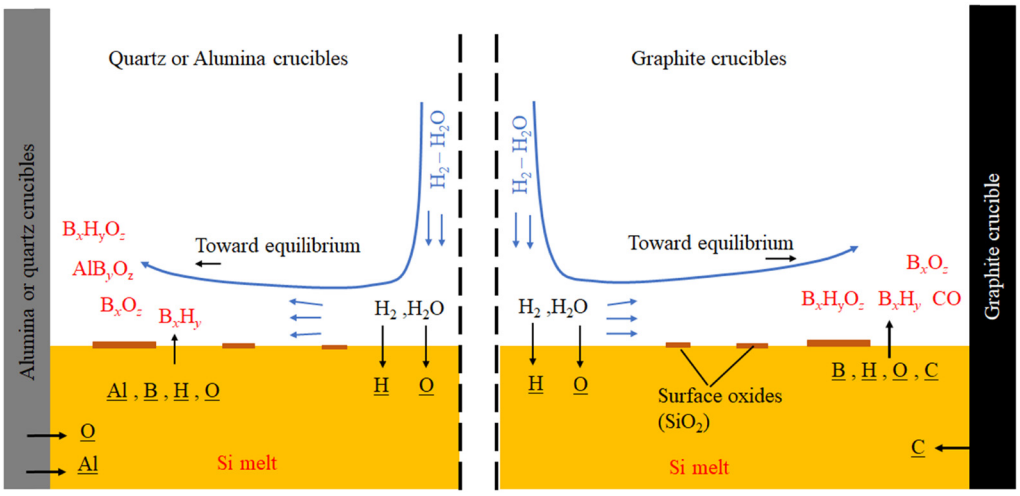

Figure 6: An illustration of the gas refining process in the quartz/alumina (left) and graphite crucibles (right), summarizing the B removal mechanisms.

almost, no B removal happened from the liquid Si. However, with the addition of humidity to hydrogen (H_2–3% H_2O), the rate of B removal increased from 0.9 to 13 μm·s^{-1} which indicates the important role of oxidation reactions on B removal from liquid Si. This indicates that the B removal mainly takes place through the formation of $B_xH_zO_y$ species and not through the BH_z compounds, and these results are in good agreement with the findings of Nordstrand and Tangstad [25] and Sortland and Tangstad [13].

From Table 4, it is obvious that the k_B in the experiment (5) is greater than the experiment (1). Both experiments were carried out at 1,500°C and with dry $H_{2(g)}$, but in alumina and graphite crucibles, respectively. These results are in good agreement with the MBMS measurements where we showed that in the case of applying alumina crucibles new volatile compounds of B like $AlBO^+$ evaporate from the melt surface, and hence the kinetics of the refining process could be accelerated in the alumina crucibles. When refining in graphite crucibles and with hydrogen gas, we can assume the B removal with BH_z compounds, and when doing the refining process in the alumina crucibles, we can assume the removal in the form of B_xO_z, $B_xO_zH_y$, and $AlBO_x$ compounds.

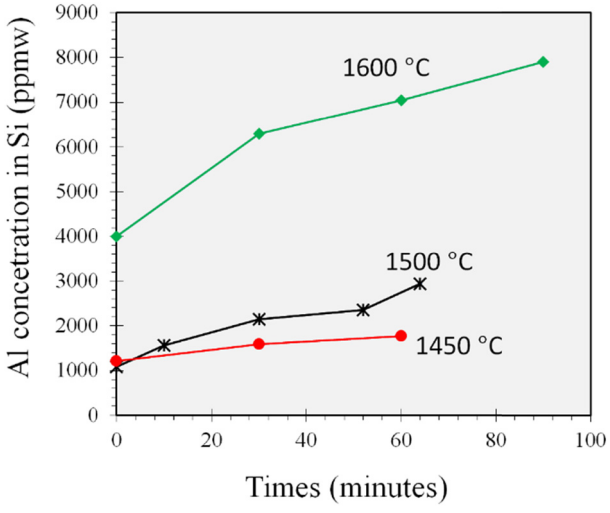

Figure 7: Aluminum concertation in liquid Si over time of gas refining.

The effect of the temperature on B removal in the alumina crucibles could also be studied by comparing the results obtained from the experiments (5–7). It is obvious that an increase in temperature leads to an increased rate of the B removal and the value of k_B increases from 1.64 to 4.15 μm·s^{-1} when the temperature is increased from 1,450 to 1,500°C, which is 2.5 times. However, when the temperature is increased to 1,600°C, the k_B equals 4.96 μm·s^{-1}. Then, beyond 1,500°C the temperature rise is no more effective for B removal. The effect of temperature is already discussed by Safarian et al. [30] indicating that when temperature increases beyond 1,500°C, silicon oxidation becomes more favorable than B oxidation reactions, leading to consumption of all the dissolved oxygen in the melt to form $SiO_{(g)}$. In experiment (7), the humidified hydrogen (H_2–3% H_2O) was applied as the refining gas and the k_B value increased to 15.3 μm·s^{-1}. A comparison of the experiment (7) with experiment (8) makes it clear that when humidity is added to the refining gas, the rate of B removal has increased almost three times. This indicates that although the alumina crucibles

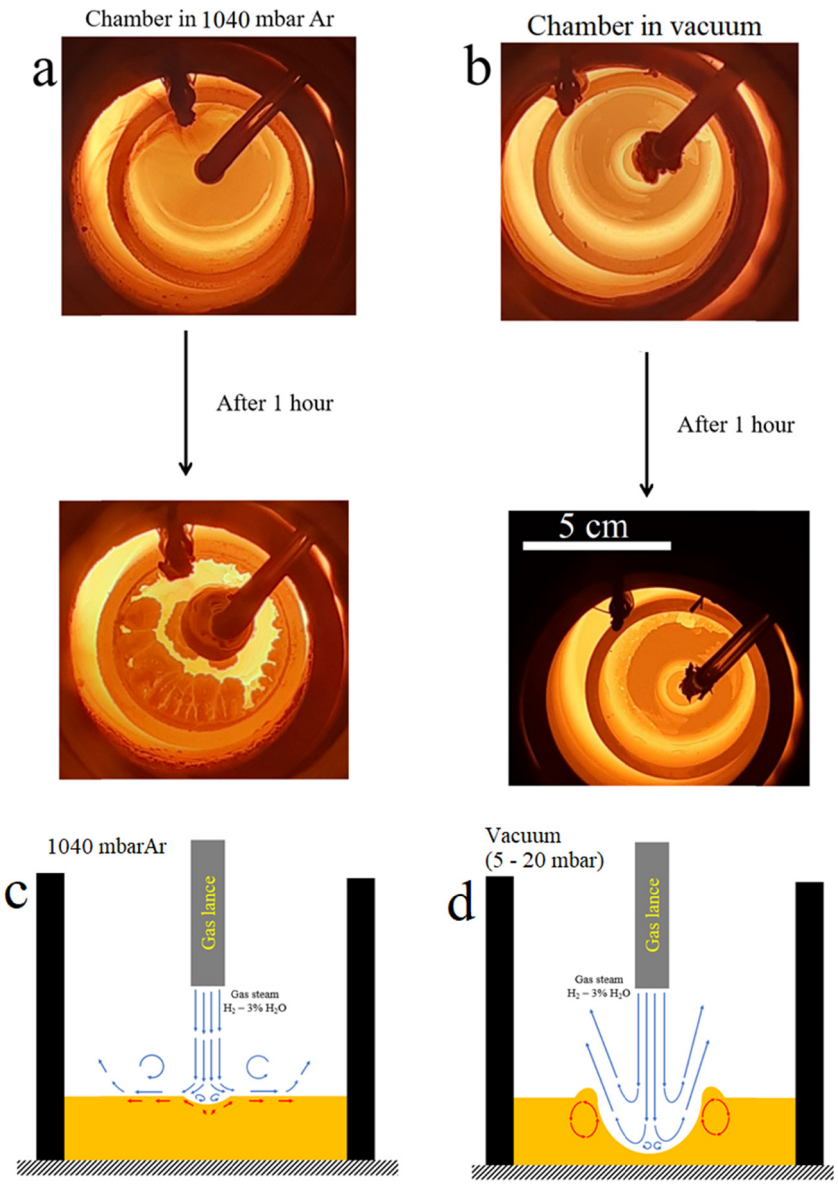

Figure 8: Photographs of the crucible during the (vacuum) refining experiments. (a) and (c) Gas refining in Ar atmosphere. (b) and (d) Gas refining in vacuum.

can supply the dissolved Al and O to the melt, the oxygen dissolved from alumina is not enough, and an exterior oxygen source is required to perform the B removal from the liquid Si.

In addition, the Al dissolved from alumina crucibles was also measured and is shown in Figure 7. The following reaction can be suggested for the dissolution of Al from alumina crucible:

$$Al_2O_3 = 2\underline{Al} + 3\underline{O}. \quad (5)$$

Figure 7 indicates that the rate of Al dissolution in the liquid Si increases with temperature and proves that when melting Si in alumina boats and crucibles, there is enough Al in the liquid to form the $AlBO_x$ compounds.

4.4 Effect of chamber gas atmosphere

By comparing the results of experiments (2–4), we can study the chamber bulk gas' effect on B removal kinetics. From Table 4 it is evident that when the chamber bulk gas is changed to He, the kinetics of B removal has accelerated and the value of k_B has increased from 13 to

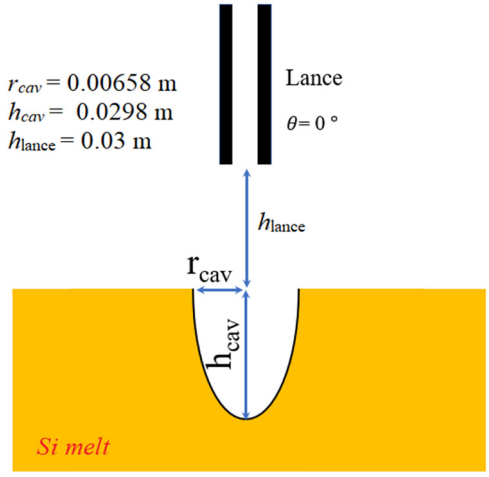

Figure 9: The calculated geometry of the impinged point on melt surface in vacuum condition, the dimensions are presented in a right scale.

17.3 μm·s^{-1}, at the same temperature accounting for 33% increase in the process rate. The positive effect of He was already reported by Safarian et al. [28] and they showed that when H_2 – 4% H_2O is mixed with He, the mass transfer coefficient of the B removal process is higher than that when mixed with Ar. He has smaller molecules compared to Ar, with He and Ar having atomic radius of 0.49 and 0.88 Å, respectively. Then, assuming the same velocity for Ar and He, the momentum of Ar molecules will go higher. The Ar and He molecules will collide with the evaporated B species from the melt surface and the higher the momentum of the foreign molecule (Ar or He), the higher the chance for bouncing the B species molecules back to the melt surface. In addition, even when the B species are successfully evaporated, they should diffuse in the gas phase to take distance from melt surface and find their way out of the crucible, unless they may return to melt through a back reaction, and this slows down the overall process kinetics for B removal. Obtaining the diffusion coefficient of the gaseous B species in the gas phase is beyond the scope of this study, but by considering the diffusion coefficient relation for gas molecules presented by Chapman and Cowling [57], we can obtain a general view about the differences between He and Ar on the diffusion of the B species in the gas phase.

$$D_{12} \propto \frac{1}{\sigma_{12}} \sqrt{\frac{1}{m_1} + \frac{1}{m_2}}, \tag{6}$$

where D denotes the diffusion coefficient, suffixes 1 and 2 indicate gas molecule 1 and gas molecule 2, m is the mass of the molecules, and σ is the average radii of the species, $\sigma_{12} = 0.5(\sigma_1 + \sigma_2)$. By assuming Ar and He as the molecule 1,

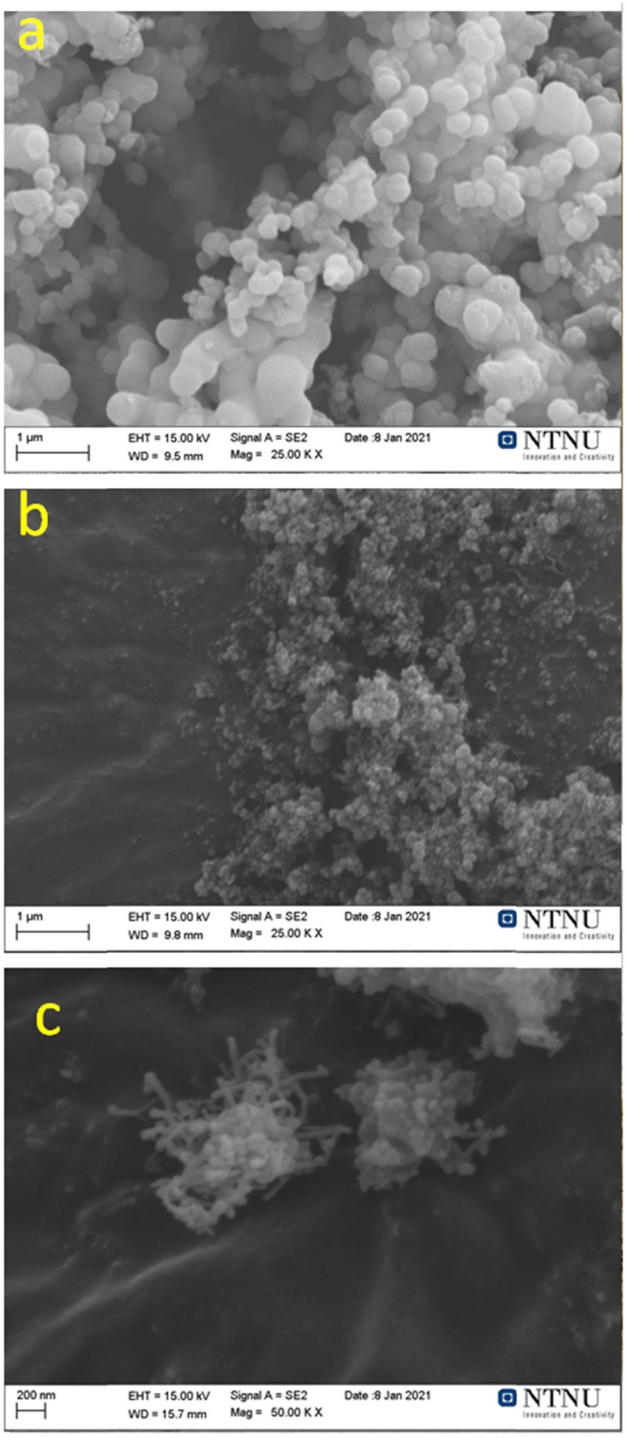

Figure 10: The SEM micrographs of the fume settled on the chamber wall: (a) He gas in the chamber, (b) Ar gas in the chamber, and (c) chamber vacuumed during the gas refining process.

and any gaseous B compound as molecule 2, then from equation (6) it is obvious that the higher the mass and diameter of the gas molecules, the lower the diffusion of the B species in the gas phase. Therefore, it is completely

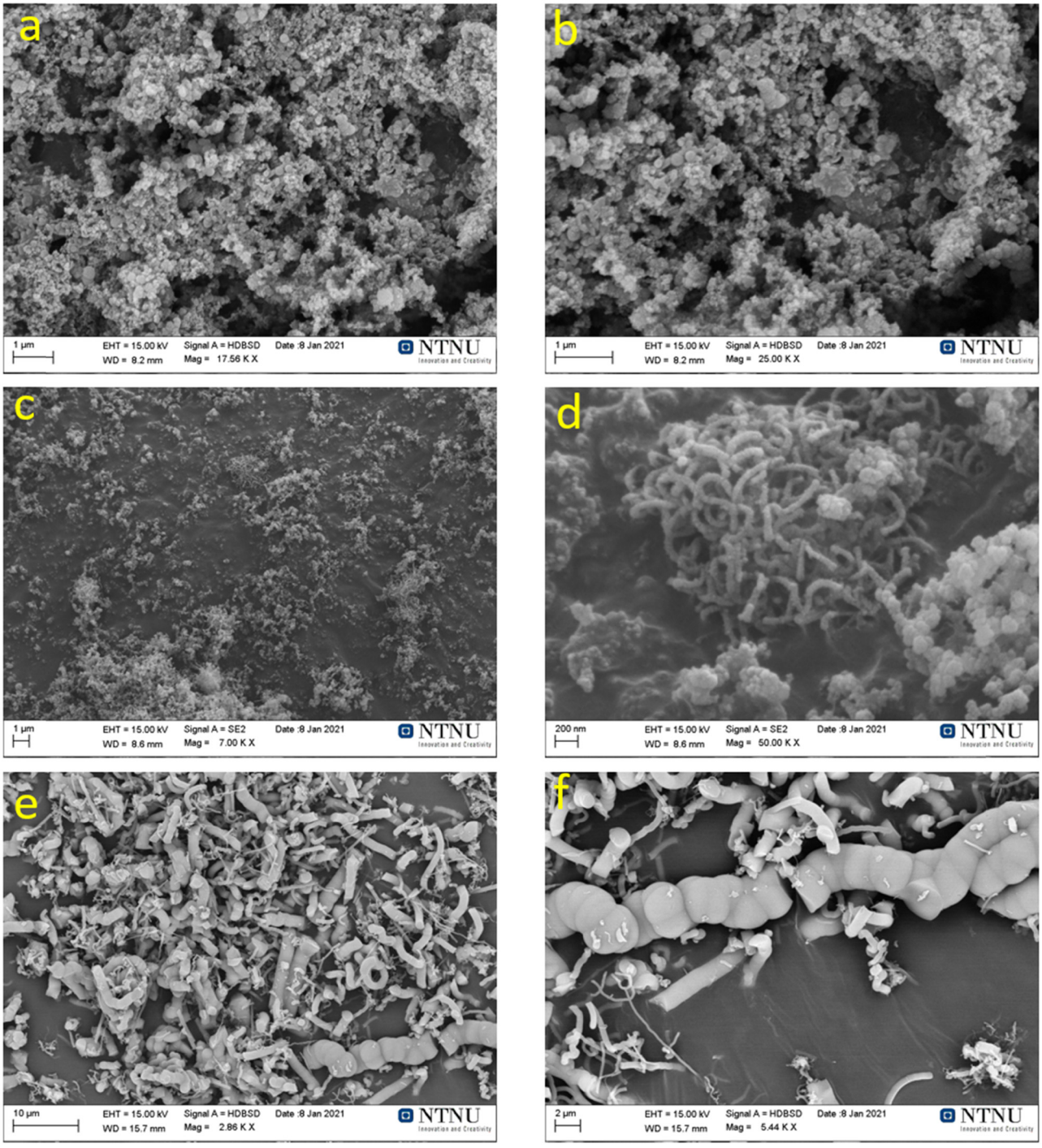

Figure 11: The SEM micrographs of the condensates settled on the gas lance: (a) and (b) He gas in the chamber, (c) and (d) Ar gas in the chamber, and (e) and (f) vacuum condition.

expectable for the same B species under study to have a higher diffusion in He than Ar. In order to accelerate the diffusion of the B species in the gas phase we carried out experiment (4); however, Table 4 indicates that when carrying out the gas refining in vacuum condition, the mass transfer coefficient for B removal has reduced to 2.56 $\mu m \cdot s^{-1}$, which was totally opposite to our expectations. In this experiment, the chamber bulk gas was continuously vacuumed during the gas refining experiment. Figure 8 compares the melt surface in experiments (3 and 5). It is obvious from Figure 8(b) and (d) that the surface of the melt has fully impinged in the case of gas blowing in vacuum condition;

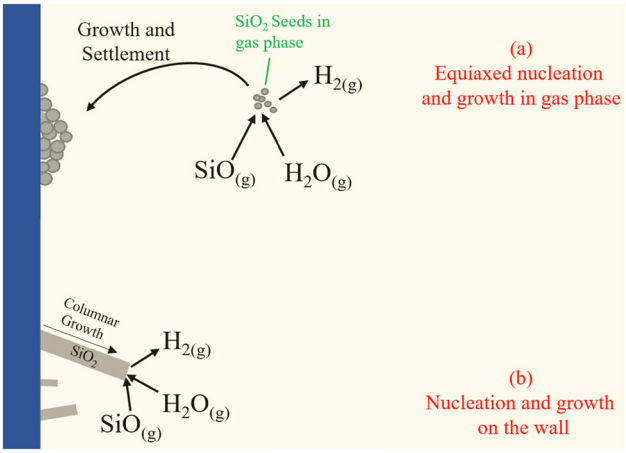

Figure 12: The schematic illustration of the silica fume formation in gas refining of Si. (a) The equiaxed growth and (b) nucleation on surface.

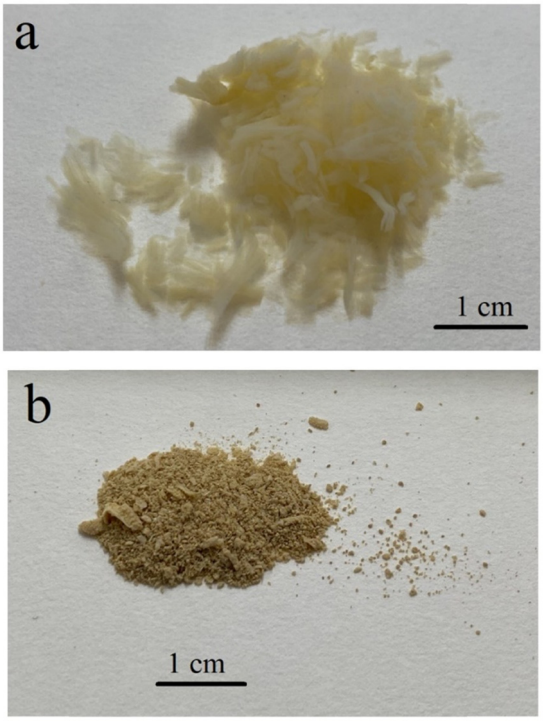

Figure 13: The photograph of the fumes collected from the chamber after gas refining. (a) In vacuum condition and (b) chamber filled with Ar gas.

however, when the chamber was in atmospheric pressure, there was no significant impinging effect on the melt surface (Figure 8[a] and [c]). Figure 8(b) and (d) also indicates that when doing the gas refining in vacuum condition there are less amounts of condensates settled on the lance and crucible compared to Ar atmosphere, and this will further be discussed in the next section.

It is worth mentioning that when carrying out the gas refining in vacuum conditions, there is almost no condensate on the lance and crucible edge. The formation of the condensates on the cold parts of the crucibles and gas lance provides practical challenges in the gas refining of Si. For example, as shown in Figure 8(a), after 60 min of the refining process, the condensates are grown from the crucible edge toward the center of the crucible, which leads to clogging the gas path toward out of the crucible, affecting the rate of the process. The fluid dynamics for melt impinging by gas blowing is already discussed and numerically simulated in refs. [58–60] and Figure 8(c) and (d) illustrates the gas fluid pattern when blowing in in gas and vacuum conditions, respectively. As shown in Figure 8(c), when the gas lance is blowing in atmospheric pressure conditions, the gas stream spreads over the melt surface. The exact fluid dynamic of the gas blowing under the experimental condition of experiment (3) is already simulated by Safarian et al. [30], and the Figure 8(c) and (d) is regenerated after their simulation results. Figure 8(d) shows the fluid pattern of gas blowing in the vacuum condition and indicates that the gas jet makes a fully impinged point on the melt surface. In the case of vacuum condition, there is less resistance due to the low pressure of the bulk gas in the chamber and this makes the velocity of the gas jet increase, leading to impinging the melt surface. As shown in Figure 8(d), when the gas jet impinges the melt surface, it splits and bounces back and then there is no further contact with the melt surface. As it is obvious in Figure 8(b), the surface area of the impinged region seems to be considerably smaller than the whole melt surface area and this means that under the conditions of experiment (5), the contact area of gas and melt is smaller than that in the other experiments. From the melt surface photograph presented in Figure 8(b), the radius of impinged point (cavity) is determined as $r_{cav} = 0.00658$ m. The impinging of melt surface with gas jets is already modeled in refs. [61,62] and here we can apply the following equations to calculate the depth of the cavity formed on the melt surface.

$$r_{cav} = 1.4065\dot{M}_d^{0.282}h_{lance}, \tag{7}$$

$$\dot{M}_d = \frac{\dot{m}_t h_{lance}}{\rho_{Si} g h^3}(1 + \sin\theta), \tag{8}$$

$$\dot{m}_n = \frac{\dot{m}_t}{n_{lance}}, \tag{9}$$

$$\dot{M}_h = \frac{\dot{m}_n \cos\theta}{\rho_{Si} g h^3}, \tag{10}$$

$$h_{cav} = 4.469\,\dot{M}_h^{0.66}h_{lance}, \tag{11}$$

where r_{cav} is the radius of the cavity or impinged area formed on the melt surface, and h_{lance} is the distance of the lance tip to the melt surface. The $\dot{M}_d$, $\dot{m}_n$, $\dot{M}_h$, and $\dot{m}_t$ are all dimensionless mass flow rates of the gas stream blowing out of the nozzle, and a full explanation for them could be found in the study by Koria and Lange [63]. n_{lance} is the number of the nozzles on the gas lance tip, and it is one in this study, θ is the inclination angle of the nozzle with the lance axis, which is zero in our case, and ρ_{Si} is the density of the liquid Si. All these parameters are shown schematically in Figure 9. By inserting the measured $r_{cav} = 0.00658$ m from Figure 8(b) in equation (7), $\dot{M}_d$ will be obtained, then $\dot{m}_t$, $\dot{m}_n$, and $\dot{M}_h$ will be obtained from equations (8–10), respectively. Finally, from equation (11), h_{cav} will be calculated as 0.0298 m. The cavity with the obtained scaled dimensions is shown in Figure 9, and as seen it has a half ellipse shape. Having the dimensions of the ellipse, we can calculate the impinged area's surface ($S_{impinged} = 0.5\pi h_{cav} r_{cav}$) as 2.17×10^{-4} m^2. Consequently, the effective A/V ratio is calculated as 2.713 m^{-1}. By correcting the A/V ratio in the first-order kinetic model for the experiment (4) carried out in vacuum condition, the effective k_B value is obtained as 23.3 μm·s^{-1}, which is 1.79 times of that when Ar was in the chamber, and 1.34 times of the case when He was in the chamber. Therefore, the effective k_B in vacuum condition shows that when the gas atmosphere in the chamber is removed by vacuuming, the rate for the vacuum refining process increases intensively. This indicates the important role of gas phase and is in good agreement with the result of the experiment (3), where He was used as chamber gas, providing higher diffusivities for the gas molecules.

4.5 Silica fume formation in gas refining

During the gas refining experiments with humidified hydrogen, $SiO_{(g)}$ forms as a product of the silicon oxidation process. The $SiO_{(g)}$ can then react with the humidity to produce small solid particles of SiO_2 and create white dust on the furnace chamber, known as silica fumes. The formation of silica fumes from the SiO gas is well discussed in the literature [26], and it could be described through the overall reaction:

$$SiO_{(g)} + H_2O_{(g)} = SiO_2 + H_{2(g)}, \quad \Delta G^{\circ}_{1,500\,^{\circ}C} = -106.9 \text{ kJ}. \tag{12}$$

The morphology of the silica fumes settled on the chamber and lance surfaces in various experiments with chamber atmosphere of Ar, He, and vacuum conditions were studied by SEM and are presented in Figures 10 and 11. Figure 10 indicates a huge difference between the sizes of the fume particles in three different experimental conditions. When He and Ar were used as the chamber bulk gas, the fume particles, settled on the chamber wall, had spherical morphology, consisting of separate spheres or several spheres attached. In addition, it is obvious from Figure 10 that the fume particles are much bigger when the chamber was filled with He gas compared to Ar and vacuum condition. The fumes settled on the chamber wall in Ar and vacuum conditions have relatively smaller sizes than in the case of He. In the case of vacuum conditions, it can be seen that some of the fume particles have grown like a comet tail. Silica fume has applications in concrete production, and the change in the morphology and size of the particles could be of interest for further study.

Figure 11(a and b) shows that the morphology of the fumes settled on the gas lance in case of the He gas is spherical but compared to the fume settled on chamber walls (Figure 10a) have considerably smaller particle sizes. However, in the case of Ar gas, some tubular morphologies could be seen among the other spheres. In the case of the vacuum condition, however, the morphology of the fumes settled on the lance is totally different, and the fume is grown in the form of whiskers and columnar morphologies. We did not find any spherical particle in the sample collected from the lance of the experiment with vacuum condition, while the fume settled on the chamber wall was spherical.

Figure 12 represents the various mechanisms for the formation of silica fumes. As it is obvious from this figure, silica fumes could form in the gas phase without any preferential nucleation site or on the body of the lance, with a preferential growth direction. When forming in gas phase, small seeds could be formed in the gas and then growing equiaxially leading to the formation of spheres. However, if the silica fume forms by initiation on a preferential nucleation site, like the lance body, then a directional growth will form the columnar morphologies and the whisker.

Considering the nucleation and growth mechanisms shown in Figure 12, the differences in the morphologies detected in the fumes could be explained. The larger sizes of the spherical particles detected in the case of He gas (in the sample collected from the chamber wall) are in good agreement with the previous discussion about the higher diffusivities of gaseous species in He compared to Ar. Having higher diffusivity, the gaseous species (SiO and H_2O) will reach the surface of the seeds faster. This leads the formation of SiO_2 seeds shown in Figure 10(a) to grow larger, before settling on the chamber wall. In the vacuum condition, however, there is lower gas density above the melt, since the chamber is being vacuumed continuously

and the pressure is in the range of 5–25 mbar. Then, the seeds formed in the gas phase on top of the melt will immediately reach the chamber wall, where they settle down. Then, similar to the case of Ar atmosphere, the silica fumes in vacuum condition will have smaller sizes. In this case, further growth on the spherical particles settled on the chamber can take place, leading to the comet tail morphologies detected in Figure 10, and schematically shown in Figure 12. In addition, when doing the vacuum refining in the vacuum condition, the velocity of the gas jet flowing out of the nozzle increases intensively (Figure 8(d)). When the gas jet impinges the melt surface and bounces back, it still has high velocity and hence will carry all the silica seeds away from the melt surface toward the chamber wall. However, the continuous gas stream over the outer surface of the gas lance provides the required gaseous reactants (SiO and H_2O) for the formation of the silica whiskers and the columns on the gas lance. The photograph of the fumes settled on the chamber wall in the two conditions, vacuum and Ar atmosphere, are shown Figure 13. As shown on this figure, the fumes collected from the experiment carried out in vacuum condition are fluffy, while in the case of Ar the fume is a fine powder.

5 Conclusion

Boron removal from Si for solar applications was studied in this research. Gas refining experiments were carried out with H_2 and H_2–3% H_2O refining gas in graphite and alumina crucibles. The MBMS was applied to characterize the off-gas of the samples in graphite, alumina, and quartz boats leading to the following remarks:

1. Refining experiments indicated higher rates of the B removal process in the alumina crucibles compared to graphite.
2. Boron removal has 33% higher process rate in He atmosphere compared to Ar and 79% higher process rate when carrying out the process in vacuum condition.
3. MBMS measurements indicated the formation of the AlBO compound, providing higher process rates.
4. HBO, HBOH (in case of graphite and quartz boats) and AlBO (in case of alumina boats) were measured experimentally by the MBMS technique.
5. The enthalpy, entropy, and C_P values for possible gaseous compounds in the H–B–Al–O system have been studied by DFT and CCSD(T) calculations.
6. The results show that the shape and size of the Silica fumes will change due to the chamber gas and atmospheric conditions. Silica fume is spherical in the case of Ar and He, and the particle size is larger in the case of Ar. In vacuum conditions, they change to the comet tail morphology.

Acknowledgements: The support from Elkem® Bremanger for Si material is highly acknowledged. The gas refining experiments done by the vacuum induction furnace were all carried out in NTNU and the hot gas characterizations by MBMS were carried out in Forschungszentrum Jülich. The authors appreciations go to Dr Lars Klemet Jakobsson from Elkem® in Kristiansand for his kind comments on the manuscript. UNINETT Sigma2 – the National Infrastructure for High Performance Computing and Data Storage in Norway is acknowledged for a generous grant of computer time (project NN9353K).

Funding information: This research was financed by the Norwegian University of Science and Technology (NTNU) and was done in cooperation with the Research Center for Sustainable Solar Cell Technology (FME SuSolTech) in Norway and the institute for energy and climate research (IEK-2), Forschungszentrum Jülich in Germany.

Author contributions: Arman Hoseinpur performed the experiments of gas refining and wrote the manuscript, Stefan Andersson carried out the theoretical calculations and drafted section two and corrected manuscript, Michael Müller performed the MBMS measurements, analyzed the MBMS data and corrected the manuscript, Kai Tang contributed significantly to ICP-MS measurements and revised the manuscript, Jafar Safarian supervised the research and revised the manuscript.

Conflict of interest: Authors state there is no conflict of interest.

References

[1] Wilson, G. M., M. Al-Jassim, W. K. Metzger, S. W. Glunz, P. Verlinden, G. Xiong, et al. The 2020 photovoltaic technologies roadmap. *Journal of Physics D: Applied Physics*, Vol. 53, No. 49, 2020, id. 493001. doi: 10.1088/1361-6463/ab9c6a.

[2] IRENA. Future of Solar Photovoltaic: Deployment, Investment, Technology, Grid Integration and Socio-Economic Aspects, 2019.

[3] Yang, D. Handbook of photovoltaic silicon, handbook of photovoltaic silicon, Springer Berlin Heidelberg, Berlin, Heidelberg, 2019, pp. 1–841.

[4] Philips, D. S. and W. Warmuth. Photovoltaics report. *PSE Conferences and Consulting Gmbh*, Freiburg, 2019.

[5] Thomas, S., M. Barati, and K. Morita. A review of slag refining of silicon alloys. *Jom*, Vol. 73, No. 1, 2021, pp. 282–292. doi: 10.1007/s11837-020-04474-0.

[6] Safarian, J. Thermochemical aspects of boron and phosphorus distribution between silicon and BaO-SiO_2 and CaO-BaO-SiO_2 slags. *Silicon*, Vol. 11, No. 1, 2019, pp. 437–451. doi: 10.1007/s12633-018-9919-8.

[7] Hosseinpour, A. and L. Tafaghodi Khajavi. Phosphorus removal from Si-Fe alloy using SiO_2-Al_2O_3-CaO slag. *Metallurgical and Materials Transactions B*, Vol. 50, No. 4, 2019, pp. 1773–1781. doi: 10.1007/s11663-019-01586-0.

[8] Baek, S. H., H. Lee, D. J. Min, S. J. Choi, B. M. Moon, and H. D. Jung. Novel recycling method for boron removal from silicon by thermal plasma treatment coupled with steam and hydrogen gases. *Metals*, Vol. 7, No. 10, 2017, id. 401. doi: 10.3390/met7100401.

[9] Yvon, A., E. Fourmond, C. Ndzogha, Y. Delannoy, C. Trassy, A. Yvon, et al. Inductive plasma process for refining of solar grade silicon. EPM 2003 4th International Conference on Electromag- Netic Processing of Materials, 2011, 125–130.

[10] Imler, W. R., R. E. Haun, R. A. Lampson, M. Charles, and P. Meese. Efficacy of plasma arc treatment for the reduction of boron in the refining of solar-grade silicon. *Conference Record of the IEEE Photovoltaic Specialists Conference*, Vol. 9718, No. 1, 2011, pp. 003435–003439. doi: 10.1109/PVSC.2011.6186685.

[11] Nakamura, N., H. Baba, Y. Sakaguchi, S. Hiwasa, and Y. Kato. Boron removal in molten silicon with steam added plasma melting method. *Journal of the Japan Institute of Metals*, Vol. 67, No. 10, 2003, pp. 583–589. doi: 10.2320/jinstmet1952.67.10_583.

[12] Alemany, C., C. Trassy, B. Pateyron, K.-I. Li, and Y. Delannoy. Refining of metallurgical-grade silicon by inductive plasma. *Solar Energy Materials and Solar Cells*, Vol. 72, No. 1–4, 2002, pp. 41–48. doi: 10.1016/S0927-0248(01)00148-9.

[13] Sortland, Ø. S. and M. Tangstad. Boron removal from silicon melts by H2O/H2 gas blowing: Mass transfer in gas and melt. *Metallurgical and Materials Transactions E*, Vol. 1, No. 3, 2014, pp. 211–225. doi: 10.1007/s40553-014-0021-x.

[14] Chen, H., X. Yuan, K. Morita, Y. Zhong, X. Ma, Z. Chen, et al. Reaction mechanism and kinetics of boron removal from molten silicon via CaO-SiO_2-$CaCl_2$ slag treatment and ammonia injection. *Metallurgical and Materials Transactions B: Process Metallurgy and Materials Processing Science*, Vol. 50, No. 5, 2019, pp. 2088–2094. doi: 10.1007/s11663-019-01639-4.

[15] Jiang, W., W. Yu, H. Qin, Y. Xue, C. Li, and X. Lv. Boron removal from silicon by hydrogen assistant during the electromagnetic directional solidification of Al–Si alloys. *International Journal of Hydrogen Energy*, Vol. 44, No. 26, 2019, pp. 13502–13508. doi: 10.1016/j.ijhydene.2019.03.248.

[16] Chen, Z., Y. You, and K. Morita. Exploration of boron removal from molten silicon by introducing oxygen resources into ammonia blowing treatment. *Canadian Metallurgical Quarterly*, Vol. 58, No. 1, 2019, pp. 82–88. doi: 10.1080/00084433.2018.1507781.

[17] Teixeira, L. A. V. and K. Morita. Removal of boron from molten silicon using CaO–SiO_2 based slags. *ISIJ International*, Vol. 49, No. 6, 2009, pp. 783–787. doi: 10.2355/isijinternational.49.783.

[18] Jakobsson, L. K. and M. Tangstad. Thermodynamics of boron removal from silicon using CaO-MgO-Al_2O_3-SiO_2 slags. *Metallurgical and Materials Transactions B*, Vol. 49, No. 4, 2018, pp. 1699–1708. doi: 10.1007/s11663-018-1250-7.

[19] Jakobsson, L. K. Distribution of boron between silicon and CaO–SiO_2, MgO–SiO_2, CaO–MgO–SiO_2 and CaO–Al_2O_3–SiO_2 slags at 1,600°C. [PhD thesis]. Norwegian University of Science and Technology (NTNU), 2013. http://hdl.handle.net/11250/249460.

[20] Bayraktar, O. Y. Possibilities of disposing silica fume and waste glass powder, which are environmental wastes, by using as a substitute for portland cement. *Environmental Science and Pollution Research*, Vol. 28, 2021, pp. 16843–16854. doi: 10.1007/s11356-020-12195-9.

[21] Golewski, G. L. and D. M. Gil. Studies of fracture toughness in concretes containing fly ash and silica fume in the first 28 days of curing. *Materials*, Vol. 14, No. 2, 2021, pp. 1–21. doi: 10.3390/ma14020319.

[22] Vikan, H. and H. Justnes. Rheology of cementitious paste with silica fume or limestone. *Cement and Concrete Research*, Vol. 37, No. 11, 2007, pp. 1512–1517. doi: 10.1016/j.cemconres.2007.08.012.

[23] Baba, H., N. Yuge, Y. Sakaguchi, M. Fukai, F. Aratani, and Y. Habu. Removal of boron from molten silicon by argon-plasma mixed with water vapor. *Tenth E.C. Photovoltaic Solar Energy Conference*, Springer Netherlands, Dordrecht, 1991, pp. 286–289.

[24] Wu, J.-J., W.-H. Ma, B. Yang, Y.-N. Dai, and K. Morita. Boron removal from metallurgical grade silicon by oxidizing refining. *Transactions of Nonferrous Metals Society of China* (*English Edition*), Vol. 19, No. 2, 2009, pp. 463–467. doi: 10.1016/S1003-6326(08)60296-4.

[25] Nordstrand, E. F. and M. Tangstad. Removal of boron from silicon by moist hydrogen gas. *Metallurgical and Materials Transactions B*, Vol. 43, No. 4, 2012, pp. 814–822. doi: 10.1007/s11663-012-9671-1.

[26] Næss, M. K., G. Tranell, J. E. Olsen, N. E. Kamfjord, and K. Tang. Mechanisms and kinetics of liquid silicon oxidation during industrial refining. *Oxidation of Metals*, Vol. 78, No. 3–4, 2012, pp. 239–251. doi: 10.1007/s11085-012-9303-9.

[27] Vadon, M., Ø. Sortland, M. Tangstad, G. Chichignoud, and Y. Delannoy. Passivation threshold for the oxidation of liquid silicon and thermodynamic non-equilibrium in the gas phase. *Metallurgical and Materials Transactions B*, Vol. 49, No. 6, 2018, pp. 3330–3342. doi: 10.1007/s11663-018-1381-x.

[28] Safarian, J., C. Sanna, and G. Tranell. Boron removal from silicon by moisturized gases. *33rd European Photovoltaic Solar Energy Conference and Exhibition BORON*, Vol. 2, No. 7491, 2016, pp. 476–479.

[29] Altenberend, J., G. Chichignoud, and Y. Delannoy. Study of mass transfer in gas blowing processes for silicon purification. *Metallurgical and Materials Transactions E*, Vol. 4, No. 1, 2017, pp. 41–50. doi: 10.1007/s40553-016-0105-x.

[30] Safarian, J., K. Tang, J. E. Olsen, S. Andersson, G. Tranell, and K. Hildal. Mechanisms and kinetics of boron removal from silicon by humidified hydrogen. *Metallurgical and Materials Transactions B*, Vol. 47, No. 2, 2016, pp. 1063–1079. doi: 10.1007/s11663-015-0566-9.

[31] Safarian, J. and M. Tangstad. Vacuum refining of molten silicon. *Metallurgical and Materials Transactions B*, Vol. 43, No. 6, 2012, pp. 1427–1445. doi: 10.1007/s11663-012-9728-1.

[32] Zhao, Y. and D. G. Truhlar. The M06 suite of density functionals for main group thermochemistry, thermochemical kinetics, noncovalent interactions, excited states, and transition elements: two new functionals and systematic testing of four

M06-class functionals and 12 other function. *Theoretical Chemistry Accounts*, Vol. 120, No. 1–3, 2008, pp. 215–241. doi: 10.1007/s00214-007-0310-x.

[33] Papajak, E. and D. G. Truhlar. Efficient diffuse basis sets for density functional theory. *Journal of Chemical Theory and Computation*, Vol. 6, No. 3, 2010, pp. 597–601. doi: 10.1021/CT900566X.

[34] Valiev, M., E. J. Bylaska, N. Govind, K. Kowalski, T. P. Straatsma, H. J. J. van Dam, et al. NWChem: A comprehensive and scalable open-source solution for large scale molecular simulations. *Computer Physics Communications*, Vol. 181, No. 9, 2010, pp. 1477–14789. doi: 10.1016/J.CPC.2010.04.018.

[35] Bartlett, R. J. and M. Musiał. Coupled-cluster theory in quantum chemistry. *Reviews of Modern Physics*, Vol. 79, No. 1, 2007, pp. 291–352. doi: 10.1103/RevModPhys.79.291.

[36] Kendall, R. A., T. H. Dunning, and R. J. Harrison. Electron affinities of the first-row atoms revisited. Systematic basis sets and wave functions. *The Journal of Chemical Physics*, Vol. 96, No. 9, 1992, pp. 6796–6806. doi: 10.1063/1.462569.

[37] Dunning, T. H., K. A. Peterson, and A. K. Wilson. Gaussian basis sets for use in correlated molecular calculations. X. The atoms aluminum through argon revisited. *The Journal of Chemical Physics*, Vol. 114, No. 21, 2001, pp. 9244–9253. doi: 10.1063/1.1367373.

[38] van Mourik, T. and T. H. Dunning. Gaussian basis sets for use in correlated molecular calculations. VIII. Standard and augmented sextuple zeta correlation consistent basis sets for aluminum through argon. *International Journal of Quantum Chemistry*, Vol. 76, No. 2, 2000, pp. 205–221. doi: 10.1002/(SICI)1097-461X(2000)76:2##205:AID-QUA10$$3.0.CO;2-C.

[39] Peterson, K. A. and T. H. Dunning. Accurate correlation consistent basis sets for molecular core–valence correlation effects: the second row atoms Al–Ar, and the first row atoms B–Ne revisited. *The Journal of Chemical Physics*, Vol. 117, No. 23, 2002, pp. 10548–10560. doi: 10.1063/1.1520138.

[40] Feller, D., K. A. Peterson, and J. Grant Hill. On the effectiveness of CCSD(T) complete basis set extrapolations for atomization energies. *The Journal of Chemical Physics*, Vol. 135, No. 4, 2011, id. 044102. doi: 10.1063/1.3613639.

[41] Martin, J. M. L. Ab initio total atomization energies of small molecules - towards the basis set limit. *Chemical Physics Letters*, Vol. 259, No. 5–6, 1996, pp. 669–678. doi: 10.1016/0009-2614(96)00898-6.

[42] Dunning, T. H. Gaussian basis sets for use in correlated molecular calculations. I. The atoms boron through neon and hydrogen. *The Journal of Chemical Physics*, Vol. 90, No. 2, 1989, pp. 1007–1023. doi: 10.1063/1.456153.

[43] Woon, D. E. and T. H. Dunning. Gaussian basis sets for use in correlated molecular calculations. III. The atoms aluminum through argon. *The Journal of Chemical Physics*, Vol. 98, No. 2, 1993, pp. 1358–1371. doi: 10.1063/1.464303.

[44] Klopper, W. Simple recipe for implementing computation of first-order relativistic corrections to electron correlation energies in framework of direct perturbation theory. *Journal of Computational Chemistry*, Vol. 18, No. 1, 1997, pp. 20–27. doi: 10.1002/(SICI)1096-987X(19970115)18:1##20:AID-JCC3$$3.0.CO;2-1.

[45] Stopkowicz, S. and J. Gauss. Relativistic corrections to electrical first-order properties using direct perturbation theory. *The Journal of Chemical Physics*, Vol. 129, No. 16, 2008, id. 164119. doi: 10.1063/1.2998300.

[46] Matthews, D. A., L. Cheng, M. E. Harding, F. Lipparini, S. Stopkowicz, T.-C. Jagau, et al. Coupled-cluster techniques for computational chemistry: the CFOUR program package. *The Journal of Chemical Physics*, Vol. 152, No. 21, 2020, id. 214108. doi: 10.1063/5.0004837.

[47] McQuarrie, D. A. and J. D. Simon. Molecular thermodynamics, University Science Books, Sausalito (California), 1999.

[48] Karton, A. and J. M. L. Martin. Heats of formation of beryllium, boron, aluminum, and silicon re-examined by means of W4 theory. *The Journal of Physical Chemistry A*, Vol. 111, No. 26, 2007, pp. 5936–5944. doi: 10.1021/jp071690x.

[49] Chase, M. W. NIST-JANAF termochemical tables. *Journal of Physical and Chemical Reference Data. Monograph*, Vol. 9, 1998, id. 1.

[50] Gurvich, L. V. and I. V. Veyts. *Thermodynamic Properties of Individual Substances*, Hemisphere Publication, New York, 1989.

[51] Porter, R. F. and S. K. Gupta. Heats of formation of gaseous H_2BOH and $HB(OH)_2$. *The Journal of Physical Chemistry*, Vol. 68, No. 9, 1964, pp. 2732–2733. doi: 10.1021/j100791a511.

[52] Cox, J., D. D. Wagman, and V. Medvedev. *CODATA Key Values for Thermodynamics*, Hemisphere Publication, New York, 1989.

[53] Hoseinpur, A. and J. Safarian. Mechanisms of graphite crucible degradation in contact with Si–Al melts at high temperatures and vacuum conditions. *Vacuum*, Vol. 171, 2020, id. 108993. doi: 10.1016/j.vacuum.2019.108993.

[54] Wolf, K. J., A. Smeda, M. Müller, and K. Hilpert. Investigations on the influence of additives for SO_2 reduction during high alkaline biomass combustion. *Energy and Fuels*, Vol. 19, No. 3, 2015, pp. 820–824. doi: 10.1021/ef040081a.

[55] Sakai, S. and K. D. Jordan. Structures and vibrational frequencies of HBeOH, HBOH, HCOH, HMgOH, HAlOH, and HSiOH. *Chemical Physics Letters*, Vol. 130, No. 1–2, 1986, pp. 103–110. doi: 10.1016/0009-2614(86)80434-1.

[56] Safarian, J., K. Tang, K. Hildal, and G. Tranell. Boron removal from silicon by humidified gases. *Metallurgical and Materials Transactions E*, Vol. 1, No. 1, 2014, pp. 41–47. doi: 10.1007/s40553-014-0007-8.

[57] Chapman, S. and T. G. Cowling. *The mathematical theory of non-uniform gases*, D. Burnet, Ed., Cambridge University Press, Cambridge, 1991, pp. 93–96.

[58] Muñoz-Esparza, D., J. M. Buchlin, K. Myrillas, and R. Berger. Numerical investigation of impinging gas jets onto deformable liquid layers. *Applied Mathematical Modelling*, Vol. 36, No. 6, 2012, pp. 2687–2700. doi: 10.1016/j.apm.2011.09.052.

[59] Nguyen, A. V. and G. M. Evans. Computational fluid dynamics modelling of gas jets impinging onto liquid pools. *Applied Mathematical Modelling*, Vol. 30, No. 11, 2006, pp. 1472–1484. doi: 10.1016/j.apm.2006.03.015.

[60] Standish, N. and Q. L. He. Drop generation due to an in the steelmaking vessel impinging jet and the effect of bottom blowing in the steel making vessel. *ISIJ International*, Vol. 29, No. 6, 1984, pp. 455–461. doi: 10.2355/isijinternational.29.455.

[61] Visuri, V.-V., M. Järvinen, J. Savolainen, P. Sulasalmi, E.-P. Heikkinen, and T. Fabritius. A mathematical model for the reduction stage of the AOD process. Part II: model validation

and results. *ISIJ International*, Vol. 53, No. 4, 2013, pp. 613–621. doi: 10.2355/isijinternational.53.613.

[62] Visuri, V.-V., M. Järvinen, P. Sulasalmi, E.-P. Heikkinen, J. Savolainen, and T. Fabritius. A mathematical model for the reduction stage of the AOD process. Part I: derivation of the model. *ISIJ International*, Vol. 53, No. 4, 2013, pp. 603–612. doi: 10.2355/isijinternational.53.603.

[63] Koria, S. C. and K. W. Lange. Penetrability of impinging gas jets in molten steel bath. *Steel Research*, Vol. 58, No. 9, 1987, pp. 421–426. doi: 10.1002/srin.198700241.

Appendix

Table A1 shows the concentration of B measured by ICP-MS at various times during the gas refining process. In Tables A2 and A3, fits to the calculated thermodynamic quantities are presented, based on the M06-2X and CCSD (T) calculations, respectively. The parameters (a_1, a_2, ..., a_7) are for the NASA polynomial functional form as:

$$\frac{C_p}{R} = a_1 + a_2T + a_3T^2 + a_4T^3 + a_5T^4, \quad \text{(A1)}$$

$$\frac{H}{RT} = a_1 + a_2\frac{T}{2} + a_3\frac{T^2}{3} + a_4\frac{T^3}{4} + a_5\frac{T^4}{5} + \frac{a_6}{T}, \quad \text{(A2)}$$

$$\frac{S}{R} = a_1 \ln T + a_2T + a_3\frac{T^2}{2} + a_4\frac{T^3}{3} + a_5\frac{T^4}{4} + a_7. \quad \text{(A3)}$$

The parameters are given for fits in two temperature ranges: 298–1,000 K and 1,000–3,500 K.

Table A1: The concentration of boron measured by ICP–MS at various times during the gas refining

Experiment number and conditions	Refining time (t, minutes) and B concentration (CB, ppmw)				
1 (graphite, H_2 in Ar, 1,500°C)	t = 0	t = 10	t = 33	t = 50	
	CB = 15.70	CB = 15.64	CB = 14.59	CB = 14.62	
2 (graphite, H_2–3% H_2O in Ar, 1,500°C)	t = 0	t = 40	t = 78	t = 98	
	CB = 9.21	CB = 3.82	CB = 2.32	CB = 1.32	
3 (graphite, H_2–3% H_2O in He, 1,500°C)	t = 0	t = 30	t = 65	t = 100	
	CB = 11.77	CB = 6.65	CB = 2.1	CB = 0.9	
4 (graphite, H_2–3% H_2O in vacuum, 1,500°C)	t = 0	t = 30	t = 55		
	CB = 11.85	CB = 10.95	CB = 9.44		
5 (alumina, H_2 in Ar, 1,450°C)	t = 0	t = 30	t = 60		
	CB = 17.18	CB = 15.38	CB = 14.70		
6 (alumina, H_2 in Ar, 1,500°C)	t = 0	t = 10	t = 30	t = 52	t = 62
	CB = 17.07	CB = 16.00	CB = 13.14	CB = 12.10	CB = 10.33
7 (alumina, H_2 in Ar, 1,600°C)	t = 0	t = 30	t = 60	t = 90	t = 120
	CB = 14.70	CB = 10.07	CB = 9.26	CB = 7.75	CB = 6.3
8 (alumina, H_2–3% H_2O, in Ar, 1,500°C)	t = 0	t = 20	t = 60		
	CB = 17.44	CB = 10.62	CB = 3.59		

Table A2: Thermodynamic data (based on M06-2X calculations) as parameters for NASA polynomials

	a_1	a_2	a_3	a_4	a_5	a_6	a_7
HBO							
298–1,000 K	2.192686×10^{00}	9.051491×10^{-03}	$-1.007469 \times 10^{-05}$	7.108782×10^{-09}	$-2.160175 \times 10^{-12}$	-2.986665×10^{04}	9.540324×10^{00}
1,000–3,500 K	3.214183×10^{00}	4.641432×10^{-03}	$-2.175393 \times 10^{-06}$	4.850579×10^{-10}	$-4.192093 \times 10^{-14}$	-3.008395×10^{04}	4.622818×10^{00}
H_2BO							
298–1,000 K	2.338867×10^{00}	1.080959×10^{-02}	$-6.917617 \times 10^{-06}$	2.005208×10^{-09}	$-1.285423 \times 10^{-13}$	-1.123348×10^{04}	1.118782×10^{01}
1,000–3,500 K	3.741728×10^{00}	7.102868×10^{-03}	$-3.447383 \times 10^{-06}$	7.891389×10^{-10}	$-6.958257 \times 10^{-14}$	-1.164750×10^{04}	3.859177×10^{00}
***Cis*-HBOH**							
298–1,000 K	2.032732×10^{00}	1.168748×10^{-02}	$-8.077930 \times 10^{-06}$	1.819725×10^{-09}	3.526881×10^{-13}	-1.017678×10^{04}	1.315776×10^{01}
1,000–3,500 K	3.962777×10^{00}	5.961031×10^{-03}	$-2.616845 \times 10^{-06}$	5.570540×10^{-10}	$-4.657031 \times 10^{-14}$	-1.066841×10^{04}	3.341731×10^{00}
***Trans*-HBOH**							
298–1,000 K	2.034096×10^{00}	1.148565×10^{-02}	$-7.475187 \times 10^{-06}$	1.115573×10^{-09}	6.298503×10^{-13}	-1.076126×10^{04}	1.313388×10^{01}
1,000–3,500 K	3.989144×10^{00}	5.854720×10^{-03}	$-2.544610 \times 10^{-06}$	5.377842×10^{-10}	$-4.472614 \times 10^{-14}$	-1.126497×10^{04}	3.155367×10^{00}
H_2BOH							
298–1,000 K	1.551882×10^{00}	1.228854×10^{-02}	3.693286×10^{-08}	$-8.297778 \times 10^{-09}$	4.112447×10^{-12}	-3.607081×10^{04}	1.527393×10^{01}
1,000–3,500 K	3.407264×10^{00}	9.881576×10^{-03}	$-4.487463 \times 10^{-06}$	9.807335×10^{-10}	$-8.366881 \times 10^{-14}$	-3.669478×10^{04}	5.082490×10^{00}
AlOB							
298–1,000 K	4.888103×10^{00}	4.581050×10^{-03}	$-2.877943 \times 10^{-06}$	2.602405×10^{-10}	2.611103×10^{-13}	-7.071663×10^{03}	1.742569×10^{00}
1,000–3,500 K	5.970225×10^{00}	1.941380×10^{-03}	$-1.017948 \times 10^{-06}$	2.462068×10^{-10}	$-2.260333 \times 10^{-14}$	-7.393681×10^{03}	-3.947136×10^{00}
AlBO							
298–1,000 K	5.307458×10^{00}	4.067187×10^{-03}	$-5.387294 \times 10^{-06}$	4.707208×10^{-09}	$-1.701416 \times 10^{-12}$	-1.243850×10^{03}	$-9.993693 \times 10^{-01}$
1,000–3,500 K	5.715965×10^{00}	2.113971×10^{-03}	$-1.056673 \times 10^{-06}$	2.469242×10^{-10}	$-2.209826 \times 10^{-14}$	-1.339847×10^{03}	-2.965471×10^{00}
$AlBO_2$							
298–1,000 K	3.791587×10^{00}	1.754482×10^{-02}	$-2.389140 \times 10^{-05}$	1.727192×10^{-08}	$-5.096931 \times 10^{-12}$	-6.760326×10^{04}	7.391040×10^{00}
1,000–3,500 K	7.239279×10^{00}	3.995178×10^{-03}	$-2.046909 \times 10^{-06}$	4.872488×10^{-10}	$-4.422530 \times 10^{-14}$	-6.837202×10^{04}	-9.465359×10^{00}
BO							
298–1,000 K	3.871990×10^{00}	$-2.985725 \times 10^{-03}$	7.619758×10^{-06}	$-6.277562 \times 10^{-09}$	1.804076×10^{-12}	-1.079853×10^{03}	3.004375×10^{00}
1,000–3,500 K	2.878687×10^{00}	1.897566×10^{-03}	$-9.394715 \times 10^{-07}$	2.179074×10^{-10}	$-1.938733 \times 10^{-14}$	-9.342059×10^{02}	7.553180×10^{00}
BO_2							
298–1,000 K	1.889568×10^{00}	1.825942×10^{-02}	$-2.642680 \times 10^{-05}$	1.861302×10^{-08}	$-5.177116 \times 10^{-12}$	-3.539771×10^{04}	1.253626×10^{01}
1,000–3,500 K	6.059342×10^{00}	1.902560×10^{-03}	$-1.023704 \times 10^{-06}$	2.520001×10^{-10}	$-2.342658 \times 10^{-14}$	-3.630803×10^{04}	-7.752557×10^{00}
BH							
298–1,000 K	3.692089×10^{00}	$-1.295861 \times 10^{-03}$	2.470678×10^{-06}	$-8.474909 \times 10^{-10}$	$-1.187262 \times 10^{-13}$	5.214727×10^{04}	$-1.020868 \times 10^{-01}$
1,000–3,500 K	2.681248×10^{00}	1.926903×10^{-03}	$-8.820968 \times 10^{-07}$	1.923252×10^{-10}	$-1.628899 \times 10^{-14}$	5.238393×10^{04}	4.962222×10^{00}
BH_2							
298–1,000 K	3.573760×10^{00}	2.255645×10^{-03}	$-1.291981 \times 10^{-06}$	1.869105×10^{-09}	$-9.248958 \times 10^{-13}$	3.550450×10^{04}	2.343090×10^{00}
1,000–3,500 K	2.617657×10^{00}	4.453314×10^{-03}	$-1.972256 \times 10^{-06}$	4.188262×10^{-10}	$-3.473053 \times 10^{-14}$	3.577305×10^{04}	7.350889×10^{00}
BH_3							
298–1,000 K	3.507845×10^{00}	$-4.731541 \times 10^{-05}$	1.267547×10^{-05}	$-1.315187 \times 10^{-08}$	4.349392×10^{-12}	9.211329×10^{03}	2.199403×10^{00}
1,000–3,500 K	1.813296×10^{00}	8.772426×10^{-03}	$-4.069795 \times 10^{-06}$	8.992461×10^{-10}	$-7.711064 \times 10^{-14}$	9.450423×10^{03}	9.880622×10^{00}

(*Continued*)

Table A2: *Continued*

	a_1	a_2	a_3	a_4	a_5	a_6	a_7
B_2O							
298–1,000 K	5.125271×10^{00}	9.296838×10^{-05}	8.772230×10^{-06}	$-1.124201 \times 10^{-08}$	4.265168×10^{-12}	1.716147×10^{04}	$-4.846355 \times 10^{-01}$
1,000–3,500 K	5.549808×10^{00}	2.490519×10^{-03}	$-1.311315 \times 10^{-06}$	3.180760×10^{-10}	$-2.926215 \times 10^{-14}$	1.686821×10^{04}	-3.553158×10^{00}
B_2O_2							
298–1,000 K	3.792476×10^{00}	1.740691×10^{-02}	$-2.721236 \times 10^{-05}$	2.297527×10^{-08}	$-7.645158 \times 10^{-12}$	-5.667889×10^{04}	3.971579×10^{00}
1,000–3,500 K	6.390474×10^{00}	4.833182×10^{-03}	$-2.404358 \times 10^{-06}$	5.600885×10^{-10}	$-5.001756 \times 10^{-14}$	-5.717459×10^{04}	-8.231215×10^{00}
B_2O_3							
298–1,000 K	2.814090×10^{00}	2.561257×10^{-02}	$-3.565608 \times 10^{-05}$	2.698822×10^{-08}	$-8.319591 \times 10^{-12}$	-1.052014×10^{05}	1.194845×10^{01}
1,000–3,500 K	7.395180×10^{00}	6.734240×10^{-03}	$-3.403456 \times 10^{-06}$	8.022708×10^{-10}	$-7.229531 \times 10^{-14}$	-1.061972×10^{05}	-1.027722×10^{01}
HOBO							
298–1,000 K	2.152567×10^{00}	1.703298×10^{-02}	$-2.179824 \times 10^{-05}$	1.496985×10^{-08}	$-4.150940 \times 10^{-12}$	-3.630995×10^{04}	1.264842×10^{01}
1,000–3,500 K	5.244871×10^{00}	4.536541×10^{-03}	$-1.944264 \times 10^{-06}$	4.071948×10^{-10}	$-3.367186 \times 10^{-14}$	-3.695483×10^{04}	-2.318121×10^{00}
$HB(OH)_2$							
298–1,000 K	1.734973×10^{-02}	2.932618×10^{-02}	$-2.767929 \times 10^{-05}$	1.226846×10^{-08}	$-1.688567 \times 10^{-12}$	-8.124362×10^{04}	2.302803×10^{01}
1,000–3,500 K	5.945754×10^{00}	9.676424×10^{-03}	$-4.180178 \times 10^{-06}$	8.814966×10^{-10}	$-7.331603 \times 10^{-14}$	-8.265630×10^{04}	-6.632140×10^{00}
$B(OH)_2$							
298–1,000 K	1.287905×10^{00}	2.410929×10^{-02}	$-2.689617 \times 10^{-05}$	1.493284×10^{-08}	$-3.129964 \times 10^{-12}$	-5.489053×10^{04}	1.776234×10^{01}
1,000–3,500 K	6.322698×10^{00}	5.936437×10^{-03}	$-2.390473 \times 10^{-06}$	4.752730×10^{-10}	$-3.768453 \times 10^{-14}$	-5.601149×10^{04}	-7.050924×10^{00}
$B(OH)_3$							
298–1,000 K	$-8.567872 \times 10^{-01}$	4.568938×10^{-02}	$-5.703717 \times 10^{-05}$	3.594749×10^{-08}	$-8.891439 \times 10^{-12}$	-1.248345×10^{05}	2.594829×10^{01}
1,000–3,500 K	8.739200×10^{00}	9.130390×10^{-03}	$-3.690762 \times 10^{-06}$	7.378861×10^{-10}	$-5.887490 \times 10^{-14}$	-1.268972×10^{05}	-2.092446×10^{01}
B_2H_6							
298–1,000 K	3.771767×10^{-01}	2.192913×10^{-02}	7.654154×10^{-08}	$-1.131216 \times 10^{-08}$	4.939286×10^{-12}	1.770757×10^{02}	1.926986×10^{01}
1,000–3,500 K	2.200759×10^{00}	2.246729×10^{-02}	$-1.090734 \times 10^{-05}$	2.497568×10^{-09}	$-2.202619 \times 10^{-13}$	-6.746032×10^{02}	8.313307×10^{00}

Table A3: Thermodynamic data (based on CCSD(T) calculations) as parameters for NASA polynomials

	a_1	a_2	a_3	a_4	a_5	a_6	a_7
HBO							
298–1,000 K	2.204674×10^{00}	9.511337×10^{-03}	$-1.111546 \times 10^{-05}$	8.031437×10^{-09}	$-2.461458 \times 10^{-12}$	-2.973189×10^{04}	9.427524×10^{00}
1,000–3,500 K	3.350674×10^{00}	4.516351×10^{-03}	$-2.125080 \times 10^{-06}$	4.752700×10^{-10}	$-4.117008 \times 10^{-14}$	-2.997224×10^{04}	3.924689×10^{00}
H_2BO							
298–1,000 K	2.398786×10^{00}	1.068061×10^{-02}	$-6.758193 \times 10^{-06}$	1.971156×10^{-09}	$-1.555221 \times 10^{-13}$	-9.448668×10^{03}	1.091219×10^{01}
1,000–3,500 K	3.781941×10^{00}	7.102937×10^{-03}	$-3.463388 \times 10^{-06}$	7.954741×10^{-10}	$-7.031671 \times 10^{-14}$	-9.864376×10^{03}	3.658347×10^{00}
***Cis*-HBOH**							
298–1,000 K	2.010623×10^{00}	1.177298×10^{-02}	$-8.074977 \times 10^{-06}$	1.730109×10^{-09}	3.970424×10^{-13}	-7.282468×10^{03}	1.327190×10^{01}
1,000–3,500 K	3.979889×10^{00}	5.981595×10^{-03}	$-2.639650 \times 10^{-06}$	5.642779×10^{-10}	$-4.733128 \times 10^{-14}$	-7.787455×10^{03}	3.241731×10^{00}
***Trans*-HBOH**							
298–1,000 K	2.013771×10^{00}	1.151420×10^{-02}	$-7.339242 \times 10^{-06}$	9.032882×10^{-10}	7.158498×10^{-13}	-8.107052×10^{03}	1.324632×10^{01}
1,000–3,500 K	3.991013×10^{00}	5.895086×10^{-03}	$-2.577275 \times 10^{-06}$	5.472420×10^{-10}	$-4.568047 \times 10^{-14}$	-8.620708×10^{03}	3.134805×10^{00}
H_2BOH							
298–1,000 K	1.547553×10^{00}	1.216517×10^{-02}	5.124492×10^{-07}	$-8.789351 \times 10^{-09}$	4.278505×10^{-12}	-3.428123×10^{04}	1.532063×10^{01}
1,000–3,500 K	3.390419×10^{00}	9.968311×10^{-03}	$-4.550637 \times 10^{-06}$	9.984243×10^{-10}	$-8.542722 \times 10^{-14}$	-3.491191×10^{04}	5.147095×10^{00}
AlOB							
298–1,000 K	4.920185×10^{00}	4.483624×10^{-03}	$-2.540733 \times 10^{-06}$	$-1.751085 \times 10^{-10}$	4.411304×10^{-13}	-4.957617×10^{03}	2.234465×10^{00}
1,000–3,500 K	6.023645×10^{00}	1.881659×10^{-03}	$-9.894724 \times 10^{-07}$	2.398008×10^{-10}	$-2.204734 \times 10^{-14}$	-5.288261×10^{03}	-3.584142×10^{00}
AlBO							
298–1,000 K	5.278695×10^{00}	4.016536×10^{-03}	$-4.785272 \times 10^{-06}$	3.875755×10^{-09}	$-1.366362 \times 10^{-12}$	-6.237499×10^{02}	$-8.694788 \times 10^{-01}$
1,000–3,500 K	5.769408×10^{00}	2.080851×10^{-03}	$-1.051079 \times 10^{-06}$	2.475126×10^{-10}	$-2.227909 \times 10^{-14}$	-7.528781×10^{02}	-3.316339×10^{00}
$AlBO_2$							
298–1,000 K	3.945705×10^{00}	1.717656×10^{-02}	$-2.332997 \times 10^{-05}$	1.681781×10^{-08}	$-4.954623 \times 10^{-12}$	-6.493380×10^{04}	7.157441×10^{00}
1,000–3,500 K	7.347670×10^{00}	3.879522×10^{-03}	$-1.993551 \times 10^{-06}$	4.755260×10^{-10}	$-4.322536 \times 10^{-14}$	-6.569610×10^{04}	-9.493774×10^{00}
BO							
298–1,000 K	3.884928×10^{00}	$-3.201944 \times 10^{-03}$	8.507345×10^{-06}	$-7.339146 \times 10^{-09}$	2.209619×10^{-12}	7.045289×10^{01}	2.982897×10^{00}
1,000–3,500 K	2.940350×10^{00}	1.854292×10^{-03}	$-9.287805 \times 10^{-07}$	2.173253×10^{-10}	$-1.946645 \times 10^{-14}$	1.890463×10^{02}	7.208263×10^{00}
BH							
298–1,000 K	3.713848×10^{00}	$-1.477944 \times 10^{-03}$	2.971175×10^{-06}	$-1.338830 \times 10^{-09}$	4.552086×10^{-14}	5.224325×10^{04}	$-1.822718 \times 10^{-01}$
1,000–3,500 K	2.693290×10^{00}	1.938478×10^{-03}	$-8.967747 \times 10^{-07}$	1.972295×10^{-10}	$-1.682423 \times 10^{-14}$	5.247342×10^{04}	4.888887×10^{00}
BH_2							
298–1,000 K	3.558525×10^{00}	2.406046×10^{-03}	$-1.587764 \times 10^{-06}$	2.155872×10^{-09}	$-1.032333 \times 10^{-12}$	3.784084×10^{04}	2.396170×10^{00}
1,000–3,500 K	2.637682×10^{00}	4.463811×10^{-03}	$-1.988762 \times 10^{-06}$	4.244878×10^{-10}	$-3.535214 \times 10^{-14}$	3.809991×10^{04}	7.227696×10^{00}
BH_3							
298–1,000 K	3.529327×10^{00}	$-2.150277 \times 10^{-04}$	1.314701×10^{-05}	$-1.356482 \times 10^{-08}$	4.465672×10^{-12}	1.114532×10^{04}	2.119366×10^{00}
1,000–3,500 K	1.821523×10^{00}	8.831680×10^{-03}	$-4.122229 \times 10^{-06}$	9.151737×10^{-10}	$-7.877142 \times 10^{-14}$	1.137521×10^{04}	9.813695×10^{00}
B_2O							
298–1,000 K	5.210220×10^{00}	$-2.958266 \times 10^{-04}$	9.518793×10^{-06}	$-1.189647 \times 10^{-08}$	4.480348×10^{-12}	1.953675×10^{04}	9.747341×10^{-01}
1,000–3,500 K	5.562765×10^{00}	2.474265×10^{-03}	$-1.302851 \times 10^{-06}$	3.160382×10^{-10}	$-2.907563 \times 10^{-14}$	1.925514×10^{04}	-1.763733×10^{00}

(*Continued*)

Table A3: *Continued*

	a_1	a_2	a_3	a_4	a_5	a_6	a_7
B_2O_2							
298–1,000 K	4.042288×10^{00}	1.610861×10^{-02}	$-2.408586 \times 10^{-05}$	1.990104×10^{-08}	$-6.582318 \times 10^{-12}$	-5.593133×10^{04}	2.957229×10^{00}
1,000–3,500 K	6.536833×10^{00}	4.727580×10^{-03}	$-2.375651 \times 10^{-06}$	5.574733×10^{-10}	$-5.005675 \times 10^{-14}$	-5.644265×10^{04}	-8.932933×10^{00}
B_2O_3							
298–1,000 K	2.973091×10^{00}	2.521099×10^{-02}	$-3.470911 \times 10^{-05}$	2.599687×10^{-08}	$-7.963295 \times 10^{-12}$	-1.023566×10^{05}	1.125446×10^{01}
1,000–3,500 K	7.579366×10^{00}	6.562628×10^{-03}	$-3.334145 \times 10^{-06}$	7.888628×10^{-10}	$-7.128083 \times 10^{-14}$	-1.033735×10^{05}	-1.117347×10^{01}
HOBO							
298–1,000 K	2.295688×10^{00}	1.643733×10^{-02}	$-2.058085 \times 10^{-05}$	1.387339×10^{-08}	$-3.790272 \times 10^{-12}$	-6.752667×10^{04}	1.204597×10^{01}
1,000–3,500 K	5.297016×10^{00}	4.509779×10^{-03}	$-1.941185 \times 10^{-06}$	4.079875×10^{-10}	$-3.383282 \times 10^{-14}$	-6.816239×10^{04}	-2.529394×10^{00}